Master's thesis

NTNU
Norwegian University of Science and Technology
Faculty of Natural Sciences
Department of Materials Science and Engineering

Vincent Simensen

Investigating the use of dip-coating and angle dependent dip-coating for deposition and synthesis of CZTS thin films for use in PV applications

Master's thesis in MSCHEM
Supervisor: Hilde Lea Lein
June 2019

NTNU
Kunnskap for en bedre verden

Vincent Simensen

Investigating the use of dip-coating and angle dependent dip-coating for deposition and synthesis of CZTS thin films for use in PV applications

Master's thesis in MSCHEM
Supervisor: Hilde Lea Lein
June 2019

Norwegian University of Science and Technology
Faculty of Natural Sciences
Department of Materials Science and Engineering

Norwegian University of
Science and Technology

I would like to start by thanking associate professor Simona Binetti for the opportunity to travel to Milan and perform my experimental work in their laboratories at the University of Milano - Bicocca, and my initial supervisor professor Eivind Øvrelid for accepting me as a master student and providing me with the opportunity to investigate a personal technological interest. I would further like to give substantial acknowledgement to Vanira Trifiletti for helping me settle in when I arrived in Milano and aiding me in my research throughout the entire semester I was there. You made my stay a pleasure and inspiring for my research. I wish you good fortune in the future and look forward to the next time I will visit Milano.

I would like to thank my current supervisor associate professor Hilde Lea Lein for helping me accomplish this this written work with guidance and help whenever I needed it. Finally I would like to thank friends, family and loved ones who motivated and cared for me during the entirety of these two years that have passed. Thank you all.

Summary

Cu_2ZnSnS_4 (CZTS) thin films were synthesized, with fluorine doped tin oxide (FTO) on soda-lime glass (SLG) as a substrate, by means of dip-coating and angle dependent dip-coating. The experimental procedure involved using thiourea as a solution-based sulfur source for the formation of CZTS and deposited samples were annealed at 500 °C in argon atmosphere for different annealing times. The effect of withdrawal speed and annealing time was investigated for conventional dip-coating, while the effect of dip angle as well as annealing time was investigated for angle dependent dip-coating. Characterization of thin films was performed with Raman spectroscopy, X-ray diffraction, ultraviolet-visual spectroscopy, scanning electron microscopy (SEM) imaging, as well as electron dispersive X-ray spectroscopy (EDXS). The thickness of the depositions were found to increase with increased withdrawal speed and the film quality was highly dependent on the annealing time. The samples produced from conventional dip-coating reached a maximum thickness of around 790 nm after two depositions annealed 12 h for each layer, and showed an even distribution of elements but a noticeable surface porosity. The film had a estimated bandgap value of 1.31 eV, with sodium present in the sample which was believed to have been a result of diffusion from the SLG layer and the possible presence of ZnS in the bulk structure. The samples produced from angle dependent dip-coating reached a maximum thickness of around 900 nm after two depositions annealed 0.5 h for the first layer and 6 h for the second layer. The result was a compact surface with little to no crystallites on the surface, believed to have been Cu_2SnS_3 phases. The film has an estimated bandgap value of 1.52 eV and even distributions of elements with a small amount of sodium present. ZnS phases in the bulk structure were still a possibility. The experimental procedure involving the use of angle dependent dip-coating was deemed a success, considering this being the first work known to the author that employs said method for CZTS thin film synthesis.

Preface

This work was submitted as the final thesis in the Master of Science in Chemistry (MSCHEM) program for the Department of Materials Science and Engineering, Norwegian University for Science and Technology (NTNU). Most of the experimental work was done during an exchange to the Department of Materials Science and Solar Energy Research Center (MIBSOLAR), University of Milano - Bicocca (UNIMIB) in the fall of 2018 with additional characterization performed at the Department of Materials Science and Engineering, Norwegian University for Science and Technology (NTNU) during the spring of 2019. The exchange was part of a cooperative project between professors Eivind Øvrelid (SINTEF) and Simona Binetti (UNIMIB). Professor Eivind Øvrelid (SINTEF) was supervisor for this project from the fall of 2017 until the fall of 2018 where associate professor Hilde Lea Lein (NTNU) assumed the position of supervisor.

All measurements and calculations were performed by the author, except for scanning electron microscopy and EDXS measurements with the Gemini 500 equipped with the Bruker, QUANTAX in Milano, which were performed by Tiziano Catelani, as well as UV-VIS spectroscopy measurements in Trondheim which were performed by Håvard Wilson. In both instances, the author was present but not responsible for operating the instruments.

Table of Contents

Summary i

Preface ii

Table of Contents iv

Abbreviations v

1 Background 1
1.1 The world of solar cells . . . 1
1.2 Aim of the work . . . 2

2 Introduction 5
2.1 Solar power . . . 5
2.2 Solar cells . . . 8
2.2.1 Solar cell design . . . 8
2.2.2 Solar cell materials . . . 10
2.2.3 Limits to solar power . . . 11
2.3 Kesterites . . . 12
2.3.1 The kesterite structure as a photovoltaic . . . 12
2.3.2 Synthesis of Cu_2ZnSnS_4 thin films . . . 13
2.3.3 Challenges concerning sol-gel synthesis of Cu_2ZnSnS_4 thin films 14
2.4 Dip-coating . . . 17
2.4.1 Experimental features . . . 17
2.4.2 Substrate thickness by varying withdrawal speed . . . 18
2.4.3 Angle dependent dip-coating . . . 19
2.4.4 Dip-coating for deposition and synthesis of Cu_2ZnSnS_4 thin films 20

2.5 Analytic methods . . . 22
2.5.1 X-ray Diffraction . . . 22
2.5.2 Raman Spectroscopy . . . 23
2.5.3 Ultraviolet-visual Spectroscopy . . . 24
2.5.4 Scanning Electron Microscopy . . . 25
2.5.5 Energy-dispersive X-ray spectroscopy . . . 26

3 Experimental **29**
3.1 Materials . . . 29
3.2 Experimental procedure . . . 30
3.2.1 Preparation of solutions and substrates . . . 30
3.2.2 Dip-coating deposition . . . 30
3.2.3 Angle dependent dip-coating . . . 31
3.3 Characterization and instrumentation . . . 32

4 Results **35**
4.1 Dip-coating . . . 35
4.1.1 Withdrawal speed . . . 35
4.1.2 Annealing time with fixed withdrawal speed . . . 41
4.2 Angle dependent dip-coating . . . 49
4.2.1 Dip angle . . . 49
4.2.2 Annealing time with fixed dip angle . . . 56

5 Discussion **69**
5.1 Dip-coating . . . 69
5.1.1 The influence of withdrawal speed . . . 69
5.1.2 Coating composition and homogeneity . . . 70
5.2 Angle dependent dip-coating . . . 73
5.2.1 The effect of dip angle . . . 73
5.2.2 Coating composition and homogeneity . . . 73

6 Conclusion **75**

7 Further work **77**

Bibliography **79**

Appendix **85**

Symbols & Abbreviations

Symbol	Definition
M	Spectral emittance
T_B	Black body temperature
λ	Wavelength
θ_Z	Solar zenith angle
E_g	Bangap energy
$\vec{k}$	Wave vector
U_0	Vertical withdrawal speed
η	Viscosity
γ_{LV}	Surface tension
R_{vap}	Evaporation rate
h_0	Deposited film thickness
k_i	Solution constant
ρ	Fluid density
L	Substrate width
D	Collective constant for physiochemical properties
u	Withdrawal speed parallel to the substrate surface
α_s	Angle between quiescent liquid and submersed substrate
X, Y	Film coordinates relative to substrate surface
θ_s	Dip angle; angle between quiescent liquid and non-submersed substrate
θ_B	Diffraction angle; Bragg angle
d	Crystal lattice spacing
n	Integer
ν_0	Frequency of incident light
ν_1	Frequency of scattered light
I	Transmitted radiation flux
I_0	Incident radiation flux
α	Absorption coefficient
A	Absorption
l	Sample thickness
ν	Frequency of light
B	Relation constant
r	Electronic transition type
V	Acceleration voltage
$E_{kin}^{el.}$	Kinematic energy of an electron
m_e	Electron mass
v	Velocity
e	Electron charge

Abbreviation	Explanation
UNIMIB	Uniersity of Milano - Bicocca
AM	Air mass
ASTM	American Society for Testing and Materials
ISO	International Organization for Standardization
IEC	International Electrotechnical Commission
NREL	National Renewable Energy Laboratory
VB	Valence band
CB	Conduction band
CIGS	Copper indium gallium selenide
CZTS	Copper zinc tin sulfide; Cu_2ZnSnS_4
CZTSSe	Copper zinc tin sulfide selenide; $Cu_2ZnSnS_xSe_{4-x}$
CBD	Chemical bath deposition
DMSO	Dimethyl sulfoxide; $(CH_3)_2SO$
FTO	Fluorine doped tin oxide; $F:SnO_2$
TCO	Transparent conductive oxide
SLG	Soda-lime glass
MIBSOLAR	Department of Materials Science and Solar Energy Research Center
UNIMIB	University of Milano - Bicocca
IMA	Department of Materials Science and Engineering
NTNU	Norwegian University of Science and Technology
XRD	X-ray diffraction
IR	Infrared
UV-VIS	Ultraviolet-Visible
EDXS	Electron dispersive X-ray spectroscopy
SEM	Scanning electron microscopy
FWHM	Full width at half-maximum

Chapter 1

Background

1.1 The world of solar cells

The industrial revolution during the 18th and 19th centuries opened a new door for technological advancements that required the use of energy to function and perform work. Combustible fossil fuels were used to power engines for transport, manufacturing and construction that propelled the western world into the modern age of today. The advent of this modern age brought an ever increasing demand for energy and continues to be a basal necessity for modern life. An important focus of scientific research over the past century has therefore been to find more efficient methods for harvesting said energy using materials available to human kind.

Fossil fuels are an example of chemical energy that is released from chemical bonds upon combustion. Radiant energy however can be stored in photons and can travel vast distances in space without any loss of energy. The sun is therefore a renewable energy source that can constantly feed the earth with photons in the form of sunlight. Solar radiation is unequivocally responsible for life on earth as radiant energy converts into thermal energy and heats the earth to a hospitable environment, and also because plants absorb radiant energy to photosynthesize and produce oxygen. The sun may be the largest renewable energy source at our disposal and even fossil fuels, formed under immense heat and pressure in the earth's crust, are products of organic material that can only have existed with available sunlight reaching the surface of the earth. The environmental difference between harvesting energy from combusting fossil fuels or directly from sunlight, concerns the chemical byproducts from combustion of fossil fuels, along with releasing available chemical energy.

Environmental research suggests that these byproducts can in sufficient amounts affect the earths climate. Some byproducts like carbon dioxide (CO_2) or methane (CH_4) can absorb and re-emit radiation and are therefore contributing to trapping radiation in the atmosphere. Such gases have been aptly named greenhouse gases and have been accumulating to a point where the natural balance of the world's climate is at stake. If man made emissions of greenhouse gases continue at such a rate, then the end result would lead to irreversible, destructive consequences. Alternative methods of harvesting energy are therefore imperative for the well-being of our future.

According to the International Energy Agency, in 2017 around 75% of the total amount of energy produced in the world came from oil, gas and coal.[1] Although this large portion consists only of fossil fuels, scientific communities have spent over a century researching the possibility of harvesting the energy from sunlight with photovoltaic devices. Ever since the discovery of the photovoltaic effect accredited to Edmond Becquerel in 1839[2], photovoltaic cells have been constructed to convert sunlight into electricity. The most widely used photovoltaic material for solar cells today is silicone, both in its polycrystalline or monocrystalline form. [3] The latter displays the highest reported efficiency to date for a single photovoltaic material at 26,3%, while the highest reported efficiency for a polycrystalline silicon solar cell is at 22,3%[4].
Along with silicone, there are many materials that display the photovoltaic effect. Among them, kesterites have proven to be a viable and emerging photovoltaic thin film material to create solar cells from. Kesterites have been synthesized with methods both in vacuum and non-vacuum. The methods in the former category involve sputtering techniques[5][6], pulsed laser deposition[7] and thermal evaporation[8]. Synthesis in non-vacuum include blade-coating[9], spin coating[10], dip-coating[], electrodeposition[11], spray pyrolysis[12] and chemical bath deposition[13]. The economic benefit and industrial scaling of synthesis in non-vacuum are advocates for the industry to adopt the production and research of thin film solar cells. Among the non-vacuum methods, dip-coating is an efficient and relatively simple method for producing compact and uniform thin films of kesterites.[14][15][16][17][18][19]

1.2 Aim of the work

The aim of this thesis will be to investigate the optimal parameters for synthesis of thin film kesterites by dip-coating for photovoltaic applications. Parameters that will be investigated include withdrawal speed during dip-coating, annealing temperature and time and angle of substrate relative to the solution during dip-coating. The evaluation of optimal parameters is reliant on post-synthesis analysis, which includes investigating surface morphology, thin film thickness, phase purity, element distribution, as well as bandgap and absorption coefficient measurements. A successful synthesis of a kesterite thin film

would entail that the thin film is expected to be compact with little to no surface porosity, having a thickness of at least 1 μm and a phase pure strucutre. Expected bandgap values lie around 1.5 eV and absorption coefficient of $>10^4$ cm^{-1}. As a part of the thesis, an academic exchange to UNIMIB (Università degli studi di Milano) was undertaken to produce the majority of samples, as well as characterization and analysis.

Chapter 2

Introduction

2.1 Solar power

The sun is responsible for providing radiant energy to life on earth but also to maintain a viable temperature range on the surface. The radiation received from the sun can be compared to the radiation received from a black body. The black body is a theoretical body that absorbs radiation from all wavelengths, and due to the thermodynamics of thermal equilibrium, must also emit a radiation spectrum of its own depending on the temperature of the body.[20] Planck's law explains that any physical body spontaneously emits electromagnetic radiation, and this spectral emittance M can be expressed in terms of the black body temperature T_B and wavelength λ of emission:

$$M_{(\lambda,T_B)} = \frac{2\pi hc^2}{\lambda^5} \frac{1}{e^{\frac{hc}{\lambda k_B T_B}} - 1} \tag{2.1}$$

h is the Planck constant, k_B is the Boltzmann constant and c is the speed of light in the medium. The total power emitted per unit area becomes then the integral of the spectral emittance $M_{(\lambda,T_B)}$ over all wavelengths and is known as the Stefan-Boltzmann law:

$$\int_0^\infty M_{(\lambda,T_B)} d\lambda = \sigma T_B^4, \quad \sigma = \frac{2\pi^5 k_B^4}{15c^2h^3} \tag{2.2}$$

Here, σ is the Stefan-Boltzmann constant. Assuming a surface temperature of 5780 K at the sun's surface, then the radiant power density is estimated to be around 63 MW m^{-2} but the radiant power density received perpendicular to the sun at the edge of the earth's atmosphere, is considered to be constant around 1360 W m^{-2}.[21][22] This difference

in power density is due to the specific angular area of the earth, at a distance from the sun's surface, being exposed to sunlight at any given moment. The latter value has been considered as the solar constant[2], however this is not the value of solar power reaching the earth's surface.

When solar radiation passes through the atmosphere, the irradiance at the surface is significantly lower than at the edge of the atmosphere due to attenuation. Causes of attenuation involve scattering and absorption of solar radiation by the different gas molecules in the atmosphere. The constituents of the atmosphere can affect the path of incident solar radiation depending on the specific nature and densities of these gases. Thus, a longer path through the atmosphere for solar radiation will result in a larger degree of attenuation. Irradiance,being the amount of solar radiation received, will therefore be dependent on the solar zenith angle θ_z; which is the angle between the sun's zenith and its current position. A higher θ_z will thus result in a longer mean path through the atmosphere. (See fig 2.1)

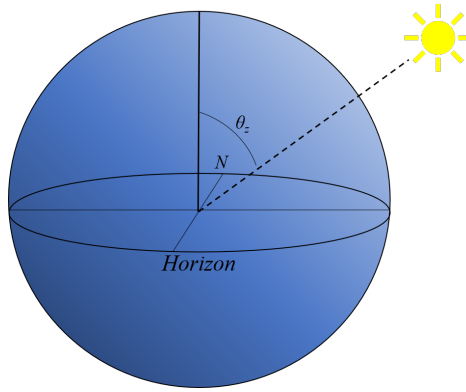

Figure 2.1: Zenith angle

The need for an agreed upon standardized value of attenuation for terrestrial radiation becomes relevant. When considering the degree of attenuation on the measured sunlight that reaches the earths surface, the Air Mass (AM) coefficient is representative and it varies accordingly:

$$AirMass = \frac{1}{cos(\theta_z)} \tag{2.3}$$

A value of AM 0 signifies irradiance without attenuation i.e at the edge of the atmosphere. AM 1 signifies irradiance from a sun at its zenith, or $\theta_z = 0°$ which would

be the shortest path of attenuation through the atmosphere. A recognized value by the scientific community for characterizing the performance of solar panels is often at AM 1,5 and therefore serves as an approximate mean value of attenuation. This value does not display the shortest path for sunlight to reach the surface of the earth, but rather at $\theta_z = 48,2°$ (See fig.2.1). AM 1,5 was adopted by the American Society for Testing and Materials (ASTM) in 1982[23], as the value corresponded more accurately with the latitude of the United States and has ever since been incorporated into international standards (ISO and IEC)[23]. The difference in terrestrial irradiance with AM 1,5 and extraterrestrial irradiance can be seen in fig.2.2

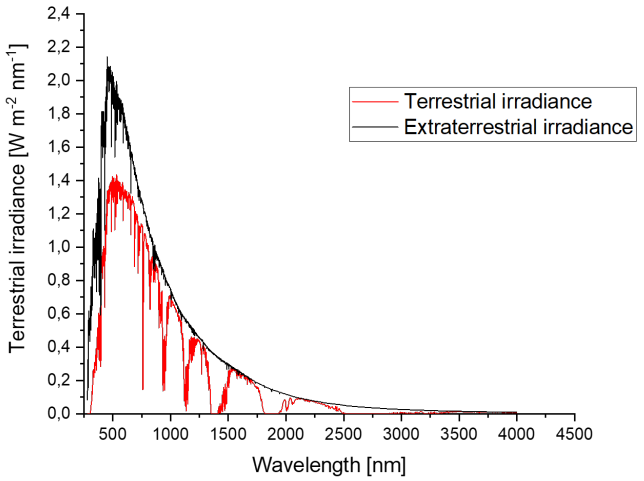

Figure 2.2: Extraterrestrial irradiance (AM 0) and terrestrial irradiance (AM 1,5) as a function of wavelength. The spectra are given by the ASTM G173-03 Standard, provided by NREL[24].

2.2 Solar cells

2.2.1 Solar cell design

The conventional solar cell is a classic example of a pn-junction, which is a contact interface between a p-type semiconductor and an n-type semiconductor.[25] Forming a pn-junction can be done by using different host materials to form a heterojunction, or by using the same host materials to form a homojunction.[2] In the case of homojunctions like crystalline silicon solar cells, the host material is doped with acceptor dopants to form a p-type semiconductor and donor dopants to form an n-type semiconductor.[2] Upon contact between a p-type and an n-type semiconductor, charge carriers like electrons and electron holes can cross the junction formed between the two semiconductors. A new pseudoregion will form around the junction, often called the depletion region which can be seen in fig. 2.3a

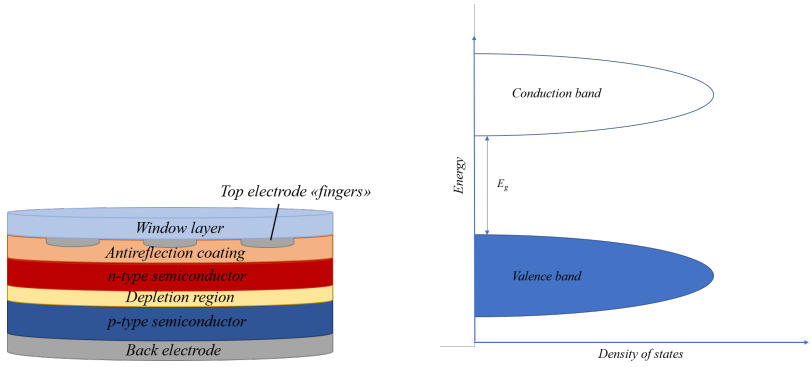

Figure 2.3: **(a)** Classical design of a solar cell. The relative thicknesses of each layer are not to scale. **(b)** Scheme of a density of states diagram for a semiconductor showing the bandgap energy E_g between the valence band (VB) and the conduction band (CB).

The name resonates the lack of charge carriers around the junction, as electrons and electron holes will recombine on both sides of the junction to form static electron-hole pairs that can no longer work as charge carriers.[2] However, if energy is supplied from a light source, electrons and electron holes can be generated from electron-hole pairs through electron excitations in the depletion region.[2] The electron-hole pairs separate to form free electrons and electron holes that become charge carriers, moving throughout the cell towards each their respective electrodes.[20] External circuitry connects the electrodes including a load which completes the circuit. The circuit load is required to match the internal resistance of the cell junction, as a measure to maximize the voltage and current

of the cell and to prevent short-circuiting from occurring at the cell junction.[20] Modern solar cell designs have the top electrode formed as lines to obstruct the least amount of solar radiation while still providing a good ohmic contact. The latter refers to a low resistance contact for major charge carriers, as they would accumulate at the surface of the region, if not given a favorable path across the electrode contact.[20] The entire cell is also covered by a protective glass layer often coated with an anti-reflection coating. The coating is a measure to trap as much sunlight as possibly that reflects off the cell before reaching the depletion region.[20] Variations on the classical solar cell include measures to increase the amount of excitations per photon, increase carrier lifetime, or increase range of susceptible wavelengths of light.[20] Other solar cell architectures vary the incident amount of radiation by reflecting sunlight onto one solar cell, called concentrator solar cells.[20]

The operating condition of a photovoltaic material is dependent on the energy gap between CB and VB of the material. This value is known as the bandgap energy E_g, and determines the energy required from incident photons to excite electrons from VB to CB.[25] as seen in fig. 2.3b. If incident photons have a wavelength that corresponds to an energy larger than the bandgap energy, then electron excitation can take place. Conduction of electrons becomes possible within the material when they are promoted from the VB to the CB, as they become delocalized in this band and can move as an electrical current.[25] Apart from the two bands being separated by different energy values, they can also have dissimilar crystal momentum which is defined by its wave vector $\vec{k}$. The wave vector is associated with the lattice electrons and belongs to their quantum mechanical wavefunction.[26] If the maximum energy value of VB coincides with the minimum of the CB, with respect to their wave vector values, then the bandgap is said to be a direct bandgap. On the other hand, if they do not coincide with respect to their wave vectors, then the bandgap is said to be an indirect bandgap. The difference can be seen in fig.2.4. For excitation to occur in indirect bandgaps, a supplementary change in crystal momentum is required. In the case of the crystal lattice, a phonon could provide the change in momentum given that a photon has provided the change in energy for the VB electron to overcome the bandgap energy. This in turn means that excitation in indirect bandgaps occurs more slowly compared to in direct bandgaps where only a photon with sufficient energy is required.[26] In the pn-junction of the solar cell, the p-type semiconductor is usually chosen as the absorbing layer of photons, based on favorable bandgap energies being in the around the electromagnetic visual range. Consequently, the p-type layer is often called the absorber layer and the n-type layer is called the window layer.[27]

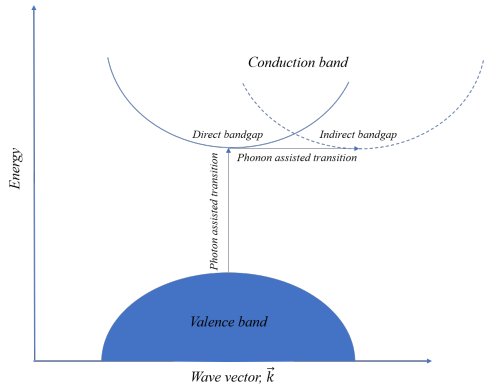

Figure 2.4: An E-$\vec{k}$ graph showing an excitation to the conduction band with a direct bandgap (solid line) and to an indirect bandgap (striped line)

2.2.2 Solar cell materials

Crystalline silicon solar cells belong to the first generation photovoltaics as they were developed and produced first. Only in the last decades have thin film solar cells been produced, which is why they have been deemed the second generation photovoltaics. As the name suggests, these photovoltaic materials do not require the same thickness as conventional silicone solar cells and include materials like CdTe, GaAs, CIGS (Copper indium gallium selenide) as well as amorphous silicon.[28] In theory, the motivation for researching thin film technologies is that the production cost would be lower than first generation photovoltaics effectively due to a decreased required amount of photovoltaic material per solar cell. Third generation photovoltaics are technologies that are designed to keep the lowered production cost of second generation, but further attempt to increase the efficiency. Emerging third generation technologies include dye-sensitized solar cells, perovskites, kesterites and tandem cells.[28][29] The idea of placing multiple photovoltaic materials in tandem to absorb a larger spectrum of the solar radiation has existed since space programs first used them in the late 1970s.[30] However the characteristics of the technology would be more natural to group in the third generation photovoltaics as record efficiencies are approaching 40% which far surpasses the theoretical limit for one photovoltaic material.[31][32] Although there is no common consensus on what separates the second and third generation of photovoltaics, the general distinction has been mentioned as the author's view on the matter. Characteristic of the third generation is also that the technologies are not yet commercially proven and are thus still in the experimental laboratory phase.

2.2.3 Limits to solar power

Due to the various factors that affect the potential radiative energy to be harnessed from the sun, a calculable theoretical limit to the maximum efficiency of a solar cell becomes relevant for . This limit is often named the Shockley-Queisser limit, accredited to the two scientists William Shockley and Hans-Joachim Queisser who postulated their calculation in 1961.[31] The Shockley-Queisser limit takes into account the black body radiation of the solar cell, the recombination of electrons and holes, the bandgap energy of the photovoltaic material and the impedance matching of a load. However according to Shockley-Queisser theory, the ultimate efficiency is reduced due to various mechanisms that result in recombination of electrons and holes and the issue is probably the most troublesome problem for any photovoltaic material.[31] Factors that can favour recombination include grain boundaries to secondary phases, impurities and defects in the crystal structure. A single junction with an absorber layer that has a bandgap of 1.1 eV will have a theoretical maximum efficiency of 30%.[31] A more recent study by Rühle[33] suggested that the theoretical efficiency is slightly higher for a material with the same bandgap. The Shockley-Queisser limit is nevertheless a frequently used value in literature to determine whether a photovoltaic material is worth investigating based on the bandgap energy.

2.3 Kesterites

2.3.1 The kesterite structure as a photovoltaic

Among the third generation photovoltaic materials, the kesterite thin film cells have generated interest and pure kesterite absorbers have proven to approach efficiencies close to 10%.[34] The kesterite structure Cu_2ZnSnS_4 (CZTS) exists naturally and crystallizes in the tetragonal crystal system.[35] CZTS is a $I_2-II-IV-VI_4$ chalcogenide semiconductor and was to the authors knowledge first presented as a photovoltaic in 1988[36]. The theoretical maximum of kesterite cells could surpass that of silicon cells, because they have direct bandgap energies in the range of around 1.0-1.5 eV and have an absorption coefficient in the range of 10^4 cm^{-1}.[27][29][37] Compared to other thin film technologies, CZTS does not contain toxic elements like arsenic or cadmium, nor rare elements like telluride or indium.[38] Its constituents are relatively abundant in the earths crust[38] and can be considered a modified version of a different chalcogenide, CIGS, where the indium and gallium have been exchanged with zinc and tin, and selenium has been exchanged with sulfur. The kesterite crystal structure (space group $I\bar{4}$) is given in fig.2.5 and has proven to be the most stable structure found by CZTS, while it has also displayed to have a stannite structure (space group $I\bar{4}2m$) and two other modifications of the kesterite structure (space groups $P\bar{4}2m$ and $P\bar{4}2c$).[39] The CZTS structure has intrinsic copper vacancies, and cation antisite defects that give rise to the p-type conductivity[40] These types of defects supply acceptor states that increase the p-type conductivity and is therefore highly sensitive to the copper concentration, with copper-poor and zinc-rich structures resulting in higher efficiencies.[27][40][41]

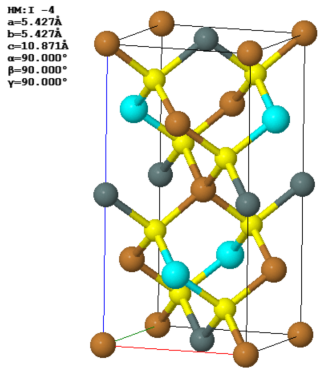

Figure 2.5: The unti cell of the tetragonal CZTS structure. Republished from The American Mineralogical Crystal Structure Database.[42]

The record efficiency of a kesterite structure was measured to 12,6%[43] and included a ratio of selenium, $Cu_2ZnSnS_xSe_{4-x}$ (CZTSSe), to tailor the bandgap value of the layer. However, the method involved the use of hydrazine (N_2H_4) as a solvent, which poses serious safety risks due to its volatile and toxic nature.[44] Due the record being set with incorporating selenium in the structure, there has been further interest to research CZTSSe structures, however the premise of achieving low-cost absorbers with abundant constituents seem lost to the author as selenium is a relatively rare element in the earths crust.[38] Focusing on producing phase pure CZTS absorber appears therefore more reasonable when trying to reach the goal low-cost absorbers. The current record for a pure CZTS is measured to 9,2% and used a sputtering technique to do so.[34] The record efficiency for a non-vacuum method is measured to 7,6% and used spin coating as the synthesis method.[45] CZTS has been produced on a laboratory scale for a couple decades and shows potential to become a viable photovoltaic material in the near future. The challenge remains however to achieve phase pure thin films that can be produced on a large scale with economic feasibility.

2.3.2 Synthesis of Cu_2ZnSnS_4 thin films

Considering the different methods of synthesis, they can be grouped into two categories; those who depend on vacuum conditions and those that do not. The existing methods used for synthesis of CZTS are adopted from production of other thin film CIGS and are therefore somewhat established. The structural similarities between CZTS and its other chalcogenide cousins like CIGS, make it possible to adopt previously used methods for thin film synthesis. CZTS synthesis that require vacuum conditions include among others various forms of sputtering[5][6], pulsed layer deposition[7] and thermal evaporation.[8] The lack of vacuum conditions for synthesis can both save production costs and simplify up-scaling processing plants, should the production of CZTS reach the market. The downside to choosing a non-vacuum method, is that a subsequent heating stage is often required for the formation of the final compound, as most vacuum methods combine deposition with recrystallization. Deposition methods used for non-vacuum synthesis of CZTS include blade-coating[9], spin coating[10], electrodeposition[11], spray pyrolysis[12], chemical bath deposition[13] and dip-coating.[14][15][16][17][18][19]

Among the non-vacuum methods, dip-coating is one of the simplest processes which makes it quite feasible to up-scale for production. The method is known to produce homogenous layers and can tailored to deposited a wide variety of purposes.[46] It can provide a more uniform spreading than tape casting by use of doctor blade, and has a faster throughput than chemical bath deposition (CBD) which can take many hours to complete. Also, there appears to be fewer articles that investigate the use of dip-coating, compared to spray pyrolysis and spin-coating. With the more manageable manufac-

turing of thin films by non-vacuum methods, comes the possibility of applying sol-gel routes to the process. The advantage of using wet chemistry like sol-gel routes, is that more control to the final composition is provided by reactant concentrations compared to electrodeposition, and solvents are easily evaporated from the deposited films. Subsequent annealing of the film allows the combination of further solvent and impurity removal, with the recrystallization of the precursors to allow growth of new compounds. Investigating the use of dip-coating with a sol-gel route for synthesis of CZTS, presents an ample opportunity for further research.

2.3.3 Challenges concerning sol-gel synthesis of Cu_2ZnSnS_4 thin films

As CZTS is a quarternary compound, the thermodynamic stability of a kesterite phase is narrowed to a relatively small window of chemical potentials in the entire phase diagram.[40][47][48] The precursor composition and reaction conditions have a strong impact when trying to form the CZTS structure and the slightest variation can lead to the formation of undesirable secondary phases including ZnS, SnS, CuS and Cu_2SnS_3.[47][48] These secondary phases can all have lower formation energies than CZTS and are therefore competing phases during the annealing stage.[40][47] Providing sulfur to the film is also a challenge particularly for non-vacuum methods. Sulfides with metallic cations typically have a low solubility in water and many organic sulfides are either corrosive, volatile and/or toxic to humans. A common experimental method applies H_2S gas during the annealing stage to sulfurize the film, as a means of a sulfur supply and/or keep the sulfur from escaping the thin film during annealing.[49][50] H_2S is however highly corrosive and is therefore not simple to handle or use in chemical synthesis. Elemental sulfur has also been used in oven chambers to provide a sulfur atmosphere during annealing[9][11][45], but molten elemental sulfur risks forming H_2S when in contact with air leakages. A more ideal method would therefore be not having to rely on these sources for sulfur, but rather on sources that can be added to the solution in the sol-gel route. Supersaturating the solution with a sulfur source followed by gentle annealing in inert atmosphere is an example of how to achieve such a method. Often, the use of sulfur vapor or H_2S during the annealing stage, is complimented by using a solution-based sulfur source. The use of the gases is justified as an assurance to prevent sulfur loss from the films.[12][50] Regardless, the circumvention of using these gases is favorable concerning safety and it has been proved possible to synthesize CZTS films without using sulfur vapor or H_2S during the annealing stage.

A viable solution-based sulfur source is thiourea ($SC(NH_2)_2$), as it is a known complexing agent and has proven to complex the metal precursors in water for use in sol-gel synthesis of CZTS.[51][52] In more recent times, Ki et al.[53] changed the solvent to dimethyl sulfoxide ($(CH_3)_2SO$), or DMSO, and Xin et al.[54] established an explicit or-

der to adding the metal precursor solutions, mixing the copper and tin solutions first. The order was established in a an attempt to fully reduce the Cu^{2+} species to Cu^{+}, which is the required copper valency in forming CZTS. The group further suggested that thiourea complexed the Cu^{+} strongly, forming a stable solution and suggested that the net redox reaction could be:

$$2\,Cu^{2+} + Sn^{2+} \longrightarrow 2\,Cu^{+} + Sn^{4+} \tag{2.4}$$

Considering how DMSO also contains sulfur, the solvent could interact with the metal ions much like thiourea, and help complex the Cu^{+} species. The mechanism of the formation of complexes was proposed to form metal sulfides during lower temperatures of the annealing, so that the same metal sulfides could act as reactants for finally forming the CZTS structure.[55] The exact chemistry of this step is however not fully understood. Other solvents that have been used for sol-gel synthesis of CZTS in conjunction with thiourea include 2-methoxyethanol,[55][56] ethanol,[17][15] and methanol;[18][57] however due to its complexing ability, the use of DMSO as a solvent with thiourea as a solution-based sulfur source are of special interest to this work. The use of additives is also frequent when applying sol-gel synthesis of CZTS. The purpose of the additive is usually to act as a surfactant, stabilizing the metal ions species and possibly control the rate of growth.[58] Other additives like sodium have been used to promote grain growth during the annealing stage.[59] Stabilizers that have been used include monoethanolamine,[17] diethanolamine,[49] and triethanolamine.[58] Recently, the use of acetylacetone as an additive has improved the performance of perovskite solar cell synthesized by a sol-gel route for spin-coating[60] Acetylacetone is a known chelating agent for transition metals for both copper(I)[61] and zinc(II).[62] The use of acetylacetone as an additive is therefore of interest to sol-gel synthesis of CZTS. Trifiletti et al.[63] reported a sol-gel route to spin-coating applying the solution mixing order of Xin et al.[54] Trifiletti et al. used thiourea as a solution-based sulfur source, DMSO as a solvent and acetylacetone as a stabilizer, and reported that their precursor solution complexed the metal ions strongly providing a stable solution for many hours on end. Their procedure for a precursor solution will therefore be applied for this work.

Annealing temperatures post deposition have been variant in literature but are generally within the 400-600 °C range for sol-gel based CZTS synthesis. The annealing temperature is often limited by the choice of substrate which can vary from soda-lime glass[49][57], to molybdenum[45][57] or fluorine doped tin oxide ($F:SnO_2$), also written as FTO.[9][64][63] Deposition on a viable back electrode material and analysis of the result is essential for a possible industrial up-scaling of CZTS production. Deposition on glass substrates is therefore, in the authors opinion, not of interest as it can not be used as a back contact electrode, as seen in fig.2.3a. The use of molybdenum (Mo) stems from past research into CIGS solar cells and its success as such,[65] however the use of more

cost-effective alternatives like a transparent conducting oxide (TCO) coated on soda-lime glass (SLG) could be a viable option. Among the TCOs, FTO has proven to have a high thermal stability and chemical stability.[66] The upper annealing temperature limit for an FTO substrate is limited by the sodium diffusion from the underlying SLG, as well as diffusion by other metals used in glass production, to temperatures above 550 °C[67]. However CZTS synthesis is typically below that limit and therefore the application of FTO is in the authors opinion of interest for CZTS film deposition and synthesis. It is clear that the combination of precursors, solvents, additives, deposition method, and substrate have a role to play on the final film quality.

2.4 Dip-coating

2.4.1 Experimental features

Dip-coating is a solution-processing method for deposition of liquid films on substrates and employs the use of a mechanical arm to dip and extract substrates at constant speeds in to one or multiple precursor solutions. Dip-coating is both a versatile and quick method to deposit films; and works in great conjuncture with sol-gel techniques.[68] Gelation of the film works as a curing process, causing the film to partially immobilize on a part of the substrate as it is withdrawn from the precursor solution. Consequently, the properties of precursor solutions are highly governing for the quality of the deposited film. The choice of solvent to the solute(s) needs to reflect the fact that the solvent should be easily removed during the subsequent annealing, as well as dissolve the solute effectively[46]. A low boiling point of the solvent permits the curing stage from being separate to the crystallization or annealing stage. Additives are also pertinent to the precursor solution, as stabilizing agents can improve the solutions properties aiding the dispersion of the solute(s) or wetting agents can increase the wetting to the substrate. Again, any additives need to be able to be burnt away without holes in the film or further affecting the morphology upon annealing[46].

The choice of substrate might not always be available to be tailored for the experiment but does play a part in the dip-coating process. The surface of the substrate should not be porous and should permit the crystallization of a film on its surface[69]. The latter can be ensured if the substrate surface and the desired thin film crystallize similarly, as to avoid detrimental dislocations or defects that can inhibit the formation of a stable thin film on the substrate. In addition, the substrate needs to be chemically resistant to the precursor solution and be able to retain its structural integrity during any further heating processes. Any substrate surface should also be cleaned prior to deposition as to avoid surface contamination[69].

When the substrate is cleaned and fastened to the mechanical arm, then it is immersed into the precursor solution. The immersion speed does not affect the applied film thickness so the speed does not have to be uniform[46]. When the substrate is immersed in the liquid, it should rest statically for small time period. The reason for the dwell time is to establish an equilibrium with substrate surface and solution, and to wait for any motion caused by the immersed substrate to settle[69]. The following withdrawal of the substrate is the experimental parameter that has the greatest effect on the film thickness.[69]

2.4.2 Substrate thickness by varying withdrawal speed

An important parameter that affects the deposition is the vertical withdrawal speed U_0, but dip-coating is also reliant on many other parameters of the precursor solution like the liquid viscosity η, surface tension γ_{LV}, evaporation rate R_{vap} to name a few. There is no equation or model that can accurately predict the thickness of a deposited film h_0, and so most models used in dip-coating are limited to specific conditions[46]. Regarding the withdrawal speed, there are four experimental regimes that represent the dependency of withdrawal speeds on the thickness of the film. At withdrawal speeds typically from 1 - 10 mm s^{-1}, the deposited film thickness h_0 can fairly accurately be described by the Landau-Levich model for a newtonian fluid and negligible evaporation, proposed by its namesakes in 1942[70]:

$$h_0 = k_i \frac{(\eta U_0)^{\frac{2}{3}}}{\gamma_{LV}^{\frac{1}{6}} (\rho g)^{\frac{1}{2}}} \tag{2.5}$$

Here, k_i is the solution constant which varies according to the ratio of solute to solvent (0.944 for Newtonian liquids[69]), ρ is the fluid density and g the acceleration of gravity. The model is a derivation of a series of equations that originate from different forces affecting the degree of draining by the liquid. Scriven[71] explained that the deposited film on the substrate is a result of liquid pulled up by the substrate, and liquid flowing down, back into the solution. The (ηU_0) represents the viscous drag caused by the moving plate while the (ρg) represents the gravitational pull on the liquid, causing the respective motions of liquid.[71] However at withdrawal speeds higher or lower than this regime, experimental data shows that the model is no longer representative for the deposited thickness.[72][73] At extreme low withdrawal speeds, the capillary action of the film will supersede as a dominating force because the evaporation rate R_{vap} is significant enough to be taken into account. This introduces the viscocapillary regime where two competing forces result in the film approaching a minimum value and increase again in thickness as withdrawal speeds further decrease decreases entering the capillary regime.[72][73] An appropriate model in the capillary regime was proposed by Faustini et al.:[73]

$$h_0 = k_i (\frac{R_{vap}}{L U_0}) \tag{2.6}$$

Here, L is the substrate width. This capillarity model[73] in conjunction with the draining model by Landau-Levich[70] forms a fairly accurate description of the intermediate viscocapillary regime between the very low and intermediate withdrawal speeds:[73]

$$h_0 = k_i (\frac{R_{vap}}{L U_0} + D {U_0}^{\frac{2}{3}}), \quad D = 0,94 \frac{\eta^{\frac{2}{3}}}{\gamma_{LV}^{\frac{1}{6}} (\rho g)^{\frac{1}{2}}} \tag{2.7}$$

Here, D is the collective constant for physiochemical properties. (See eq.2.5)
If withdrawal speeds were to be increased above the Landau-Levich region, the deposited film thickness appears to stagnate towards a maximum.[74] This might be explained by the fact that the gravitational contribution to the viscous drag is no longer counterbalanced by the adhesive forces in the liquid.[73] The film experiences therefore a shear thinning, causing the deposited film thickness to stagnate towards a maximum. An appropriate withdrawal speed when using dip-coating as a deposition method is therefore paramount for the final film quality.

2.4.3 Angle dependent dip-coating

As an alternative way of performing dip-coating, the substrate can not only be immersed in the precursor solution vertically, but also at an angle. Deryagin and Levi[75] proposed a different method to derive expressions for entrained film thickness h_0; as a function of withdrawal speed parallel to the surface u and angle α_s between a quiescent liquid surface and the submerged surface of the substrate. Their work appears to have been based on the Navier-Stokes equations in the lubrication approximation[76] and lead them to the equation:

$$\gamma_{LV}\frac{d^3h_0}{dx^3} - \rho g sin\alpha = \eta\frac{d^2u}{dy^2} \tag{2.8}$$

where h is the film thickness, x and y are the coordinates for part of the film parallel to the substrate surface and normal to the substrate surface respectively and can be seen in fig.2.6.

They proposed further a solution to the equation 2.8 by neglecting the effects of gravity and found:

$$h_0 = \frac{k_i D u^{\frac{2}{3}}}{(1 - cos\alpha_s)^{\frac{1}{2}}} \tag{2.9}$$

Further on, Bottein et al.[77] adapted the solution to a complimentary angle of α_s, namely θ_s which is the angle between a quiescent liquid surface to the non-immersed substrate surface. This is shown in fig.2.6. They also combined the equations of Faustini et al.[73] to incorporate evaporation of the liquid:

$$h_0 = \frac{k_i R_{vap} sin\theta_s}{LU_0} + \frac{k_i D {U_0}^{\frac{2}{3}})}{(sin\theta_s)^{\frac{2}{3}}(1 + cos\theta_s)^{\frac{1}{2}}} \tag{2.10}$$

Also, the withdrawal speed parallel to the substrate surface is no longer used, but the vertical withdrawal speed by substituting $u = \frac{U_0}{sin\theta_s}$. The equation2.10 refers to deposition

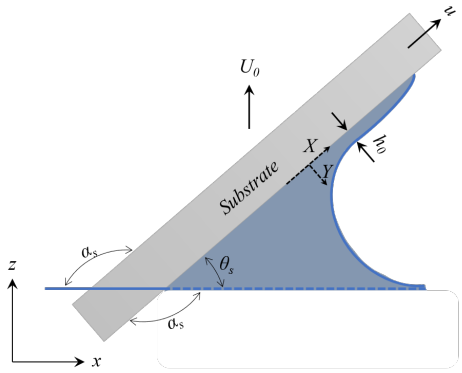

Figure 2.6: A illustration of angle dependent dip-coating

on the bottom surface of the substrate, not the top, and shows how thicker thicknesses are possible at very low θ_s angles. Arfsten et al.[78] reported stronger edge effects on films deposited on top of the substrate compared to on the bottom. The term edge effects refers to deposited liquid on the substrate dragging away from the edge, creating a region of non-homogenous thicknesses at the edge of the deposited layer. Their data however did fit the equation 2.10 within the θ_s angles they examined, which were 90°-30°, disregarding the effects of evaporation. Bottein et al. further reported that at low enough θ_s angles, the evaporation of the liquid could practically be inexistent ($R_{vap} \approx 0$) and their data also fitted the equation 2.10 for inexistent evaporation.

2.4.4 Dip-coating for deposition and synthesis of Cu_2ZnSnS_4 thin films

A large challenge concerning the use of dip-coating as a deposition method, is that the deposited films post-annealing can be relatively thin; meaning smaller than 200 nm for one deposition. This makes post-annealing analysis of the thin film difficult as the film will not produce a strong enough signal compared to the underlying crystalline FTO layer. A desirable thickness can therefore be around 1 μm to insure a detectable signal can be provided for various analytic methods. Multiple depositions would likely be required to reach such a target, but would be beneficial if kept to a minimum.

Phan et al.[14] reported a withdrawal speed of 3 cm min^{-1} and achieved around 600 nm thick CZTS layer after 10 depositions, while achieving around 940 nm thick CZTS layer after 12 depositions. The substrate was an unspecified glass substrate, and they

used thiourea as a solution-based sulfur source, with 2-methoxyethanol as solvent and triethanolamine as stabilizer. Each layer was heat treated at 250 °C for 10 min in air, and the final annealing was performed at 450 °C for 1 h in nitrogen atmosphere. Aslan et al.[15] reported a withdrawal speed of 5 cm min^{-1} and achieved a CZTS layer thickness of around 4100 nm after an undisclosed amount of depositions. The substrate used was also an unspecified glass substrate, and they used thiourea as a solution-based sulfur source, with ethanol and glacial acetic acid as solvent, and triethanolamine as stabilizer. Each layer was heat treated in air at 175 °C for 2 min and then at 300 °C for 1 min. The annealing was performed at 515 °C for 30 min in argon atmosphere. Later, the same group[16] reported the same method to achieve CZTS layer thicknesses from 650-810 nm. Sun et al.[17] reported an undisclosed withdrawal speed to achieve a CZTS layer thickness of around 1450 nm after 4 depositions. The substrate was Mo-coated SLG and they used thioacetamide as a solution-based sulfur source, with ethanol as solvent and monoethanolamine as stabilizer. Each layer was heat treated at 130 °C in air for 10 min , and the final annealing step was performed in vacuum at 480 °C for 30 min. Patel et al.[18] reported an undisclosed withdrawal speed to achieve a CZTS layer thickness of around 1500 nm after only 1 deposition, and around 3000 nm after 2 depositions. The substrate was an unspecified glass substrate and they used thiourea as a solution-based sulfur source, with methanol as a solvent and no further additives. Each layer was heat treated at 200 °for 20 min in unspecified conditions. The annealing was also reported to be performed in vacuum with elemental sulfur environment at 550 °C for an unspecified time. Chaudhuri et al.[19] reported an undisclosed withdrawal speed and achieved a CZTS layer thickness of around 450 nm after 5 depositions. The substrate used was an unspecified glass substrate and they used thiourea as a solution-based sulfur source, with methanol as solvent and no further additives. The reported only one final heat treating stage that was performed in air at 200 °C for 10 min.
Literature concerning the use of dip-coating for deposition and subsequent annealing for CZTS thin film synthesis is often lacking or questionable, specially regarding the experimental details. A detailed study, investigating the optimal parameters for a method applying a sol-gel route to dip-coating and synthesis of CZTS thin films, is therefore of interest. To the author's best knowledge, there are no articles concerning the use of angle-dependent dip-coating for deposition and synthesis of CZTS.

2.5 Analytic methods

2.5.1 X-ray Diffraction

The use of X-ray Diffraction (XRD) provides qualitative information regarding the crystal structure of a sample. Different phases, structures and crystallite sizes can be obtained using this method and has therefore made it one of the most popular methods for material analysis. The method applies Braggs law (2.11) which relates the diffraction angle θ_B of incident X-rays with wavelength λ to the spacing between atomic layers in the crystal structure d.

$$2dsin\theta_B = n\lambda \tag{2.11}$$

Here, n is an integer. When the electrons in the atoms of a crystalline sample are exposed to electromagnetic radiation they can either scatter radiation, absorb radiation or let the radiation pass depending on the energy and direction of the incoming radiation. Upon interacting with incident radiation, the atom can scatter the radiation so that the momentum is preserved but the direction changed. This is referred to as elastic scattering and is a condition that is required for Braggs law. In the case of electrons around an atom, the scattering angle θ_B relative to the atomic plane will be equal to the incident angle of radiation and are referred to as Bragg angles, seen in fig.2.7. However, for most incident angles, the scattered waves will be out of phase and produce destructive interference. Only when Braggs law is true will the scattered waves be in phase and produce intense constructive interference. This behaviour is displayed by waves, not particles, and the scattering is therefore referred to as diffraction.

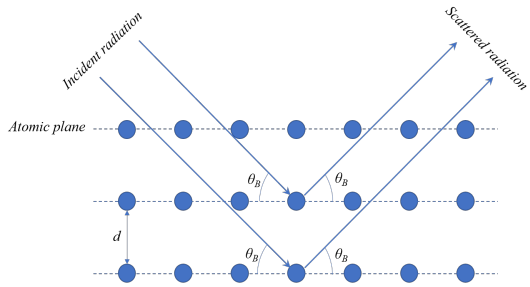

Figure 2.7: Scattering of radiation by crystal planes

A polycrystalline sample will most often have multiple peaks and it is the collection of peaks that is characteristic for each compound. In practice, each peak is associated with

a width and intensity. Phases with similar composition can crystallize similarly, which in turn can produce convoluted peaks if they exist in the same sample. Shifts in intensity and position of the peaks can therefore be attributed to secondary phases present in a sample.
The widths in peaks are due to deviations from a pure monocrystalline material which causes minute diffraction around the exact Bragg angles. The strain at grain boundaries will cause inelastic scattering and a smaller grain will therefore lead to a larger degree of additional diffraction around the Bragg angle.

2.5.2 Raman Spectroscopy

Raman spectroscopy is used to detect different crystal structures within a sample, and even separate different phases that may crystallize similarly. Polymorphs of the same compound can also be distinguished using this method.[39] When a sample is exposed to light, it might absorb some wavelengths while scattering others. The scattering can be elastic, as is the case with Rayleigh scattering, or inelastic, which is the case of Raman scattering.[25] Of the two, the latter is far less intense to measure and exhibits a shift in frequency compared to the frequency of the incident light ν_0. The shift is a result of virtual energy states that alter the frequency of the scattered light. If a molecule is promoted to a virtual energy state and then relaxes to a vibration state higher than the original vibration state, then the scattered light will have a frequency of $\nu_0 - \nu_1$, where ν_1 is the frequency difference between the two vibrations states. If the molecule is already promoted to a virtual energy state, then the scattered light will have a frequency value $\nu_0 + \nu_1$. The first case is a Stokes shift, and occurs much more often that the second case which is an Anti-Stokes shift.[25] Simply put, Raman spectroscopy measures the intensity of Raman scattering by a sample in a range of frequencies or wavelengths. Raman scattering also occurs over an interval of frequencies $\nu_0 \pm \nu_1$ which produces widened peaks in the recorded spectrum. Two or more peaks can therefore be convoluted and appear as one peak. The only peak appearing would then be shifted to a position in between the convoluted peaks.

In Raman spectroscopy, for a vibrational mode to be Raman active, meaning the specific mode appears in a Raman spectra, the nuclear vibrations involved need to cause a change in polarizability.[25] This means that polymorphs of the same compound and secondary phases that crystallize similarly can be distinguishable in a Raman spectra. Thus the method is invaluable for examining the presence of unwanted secondary phases in a thin film. Raman Spectroscopy is similar to infrared (IR) spectroscopy, as they both operate within the infrared range and target vibrational modes in molecules. The advantage of using Raman spectroscopy over IR spectroscopy in the case of analyzing CZTS

thin films is that there is no sample preparation required. In IR spectroscopy the sample needs to be in powder form and the intensity of signal needs to be taken into account to obtain tangible results.

2.5.3 Ultraviolet-visual Spectroscopy

Common to other spectroscopy methods, ultraviolet-visual (UV-VIS) spectroscopy measures the absorbance of radiation by a sample as a function of wavelength or energy within the ultraviolet and visual light range.[25] The method is also used to estimate bandgap values of semiconductors.[79] As previously mentioned, a large section of the terrestrial radiation is within the UV-VIS range. An indicator to the operational range for a photovoltaic material could therefore be found by calculating the bandgap energy of the same material. Ideally, the bandgap energy would lie somewhere around 1.5 eV, translating to wavelengths around the largest section of terrestrial irradiance, as seen in fig.2.2 The method itself targets valence electron transitions as these usually require energies that lie in the near IR and UV-VIS range. There are various transitions that can occur, like localized electron promotion within an atom and promotion to delocalized bands like in the valence band, but the type of transition that is relevant to photovoltaics is the promotion of electrons from VB to CB. In the absorption spectrum, the promotion of electrons across the bandgap is expressed as the most intense absorption peak and can only be partially seen as it crosses into a higher energy range than what the method can measure. The onset of this intense absorption is called the absorption edge. Below the absorption edge are other, smaller peaks that are associated with the other types of transitions mentioned. The attenuation of radiation can also be expressed in the form of Beer-Lambert law:

$$I = I_0 e^{-\alpha l} \tag{2.12}$$

Here, I is the transmitted radiation flux by the sample, I_0 is the initial radiation flux the sample receives, α is the absorption coefficient and l is the sample thickness. This provides the basis for constructing a formula to calculate the absorption coefficient α which indicates the degree of attenuation. A higher Since absorption $A = log\frac{I_0}{I}$:

$$\alpha = \frac{A}{l} log(e) \tag{2.13}$$

Edward A. Davis and Nevill F. Mott [80] suggested, based of the work of Tauc,[81] that amorphous semiconductors with direct bandgaps obey the relation:

$$(\alpha h\nu)^{\frac{1}{r}} = B(h\nu - E_g), \quad r = \begin{cases} \frac{1}{2} \text{for allowed transitions} \\ \\ \frac{2}{3} \text{for forbidden transitions} \end{cases} \tag{2.14}$$

B is a relation constant that is dependent on the material analyzed and can be found by fitting to the experimental data. This relation has become widely used for bandgap measurements in semiconductors, both amorphous and crystalline.[82] The r value varies depending on whether the electronic transition is allowed or forbidden, and if the bandgap is direct or indirect[82]. Considering CZTS is direct bandgap semiconductor[36] and allowed transitions occur the most, the value $r = \frac{1}{2}$ is assumed when working with CZTS. The relation also shows that upon extrapolation of the linear section of the plot to $\alpha = 0$, the intercept represents the bandgap energy E_g of the material. Such a plot is commonly named Tauc plots and are essentially an extrapolation of the absorption edge to estimate bandgap values of semiconductors.[79][82]

2.5.4 Scanning Electron Microscopy

Electron microscopy is a versatile method for imaging of samples with a resolution that far surpasses that of traditional microscopy. The method can be used for imaging of morphological and structural analysis, and works well in conjuncture with other analysis methods like electron dispersive X-ray spectroscopy (EDXS). If electron microscopy were compared to traditional microscopy, there are principal similarities between the two and terminology is often the same. [25] Instead of exposing a sample to light and using glass lenses to focus and project the image to the human eye, electron microscopy applies a stream of electrons to an exposed sample and electromagnet lenses to focus and project the stream, while using electron sensors to construct an image on a software.[83] An electron stream is produced by a source, and passed through a condenser lens which gathers the stream and converges it into further down towards the objective lens. The objective lens focuses the electron stream onto a point on the sample. A smaller electron stream diameter results in a higher resolution of the final image.[83] Objective lenses for secondary electrons also exist in different configurations. The most typical configuration is asymmetric configuration, and can be improved by applying a symemtric configuration[83] The latter is also called an in-lens, and provides a lower lens aberration. Many different configurations exist and apertures can also be applied to limit the size of the electron stream.
When a sample is exposed to an electron stream, and the energy of the incoming electrons is high enough, the sample can emit ionized electrons, also called secondary electrons. The recording of secondary electrons falls under scanning electron microscopy (SEM), along with recording back scattered electrons, and emitted X-rays by the sample.[83] Secondary electrons are produced from an inelastic process and will therefore have a much lower energy than their initial energy.[83] Due to this fact, only secondary electrons from the surface can escape the sample and be detected. Secondary electrons emitted by atoms further into the sample will have a higher certainty to dissipate into the

lattice.[25] This quality is therefore beneficial when analyzing surface topography and structure.

Electron streams in SEM are commonly either produced thermoionically or by field emission. The former applies a tungsten filament that is heated by running a current through it. Emission of electrons occurs at high temperatures due to an applied current on a filament which acts as a cathode. Charged anodic plates cause the electrons to eject from the filament and accelerate towards the plates. This however results in a relatively large energy spread among the ejected electrons, increasing chromatic aberration which is the failure of a lens to focus an electron stream due to varying wavelengths. The improved electron sources operate by field emission and can produce electrons with a smaller energy spread. In this type of electron source, a monocrystalline crystal tip is develops a strong electric field under an applied current and electrons are more easily ejected from the tip towards charged anode plates compared to thermionic sources.[83] In addition, the degree of chromatic aberration is reduced because the field emission gun produces a narrower distribution of electron wavelengths.[83] However, samples that are not good conductors of electrons can often risk building up electrons on the surface. The charge build-up results in lower quality imaging as the noise level rises accordingly.[83]

The energy of the electrons in the stream can be varied depending on the electron source and the accelerating voltage V. The kinematic energy of an electron $E_{kin}^{el.}$ can be expressed in the classical sense:

$$E_{kin}^{el.} = \frac{1}{2} m_e v^2 = eV \tag{2.15}$$

where m_e is the electron mass, e is the electron charge and v is the velocity. The relation becomes evident when considering that electrons gain kinetic when exposed to an electric field between the two electrodes. The energy gained is dependent on the potential difference between the electrodes, i.e the voltage.

2.5.5 Energy-dispersive X-ray spectroscopy

Due to the experimental conditions of SEM, auxiliary analysis can be performed by examining the emission of X-rays by a sample under electron bombardment. Energy-dispersive X-ray spectroscopy (EDXS) gives qualitative, and some quantitative analysis of elements present in a sample. The technique is useful for compounds that contain multiple elements, like kesterites, to examine the distribution of the constituents. The technique is also be used for estimating the thickness of the kesterite sample after synthesis. Every atom can produce characteristic X-rays under exposure to electrons with

high enough energy, due to core electrons (K-shell) being knocked out of their energy levels and subsequent relaxation of outer-shell electrons resulting in the emission of X-rays. Relaxation from any energy level to the K-shell is called a K_α transition and will therefore produce K_α radiation as X-rays. Subsequently, L_α radiation is a result of L-shell electrons being knocked out of their energy levels. This is why every element has characteristic K_α X-rays that can be recorded for qualitative analysis. The intensity of each peak in the recorded spectrum is consequently dependent on having an acceleration voltage high enough to ionize K-shell electrons.[25] The term energy dispersive originates from the fact that it is energies in the form of voltages, and not wavelengths that are being measured. Quantitative analysis is also possible with EDXS but depends on the calibration used to calculate relative amounts.[25]

Chapter 3

Experimental

3.1 Materials

The materials used for the precursor solution in the experimental procedure are listed in table 3.1. Materials otherwise used for the experimental procedure are listed in table 3.2

Material name	Chemical formula	Form
Copper(II) acetate monohydrate	$Cu(CH_3COO)_2 \cdot H_2O$	Powder, 99.00%
Tin(II) chloride dihydrate	$SnCl_2 \cdot 2\,H_2O$	Powder, 98.00%
Zinc(II) acetate dihydrate	$Zn(CH_3COO)_2 \cdot 2\,H_2O$	Powder, 99.99%
Thiourea	$SC(NH)_2$	Powder, 99.00%
Dimethyl sulfoxide	$(CH_3)_2SO$	Liquid, 99.9%
Acetylacetone	$CH_3COCH_2COCH_3$	Liquid, $\geqslant$ 99%

Table 3.1: Materials used for the precursor solution. All chemicals for synthesis were supplied by Sigma Aldrich except for the copper(II) acetate which was supplied by Merck

Material name	Chemical formula	Note
Fluorine doped tin oxide	F:SnO_2	Coated on soda-lime glass, TEC 7 standard
Mucasol	-	Universal detergent solution
Distilled water	H_2O	-
Acetone	CH_3COCH_3	Liquid, $\geqslant$ 99.9%
Ethanol	C_2H_5OH	Liquid, Reagent grade
Alumina	Al_2O_3	Solid, Precursor solution container
Aluminium	Al	Solid
Kapton FN	-	Polyimide tape, DuPont
Nitrogen	N_2	Gas
Argon	Ar	Gas

Table 3.2: Supplementary materials used to complete the experimental procedure

3.2 Experimental procedure

3.2.1 Preparation of solutions and substrates

Stock solutions of 0.250 M copper(II) acetate monohydrate, 0.125 M tin(II) chloride dihydrate, 0.125 M zinc acetate dihydrate, and 2.5 M thiourea were prepared with dimethyl sulfoxide (DMSO) as the solvent. Each solution was stirred on a magnetic stirrer for 24 h at 298 K. 100 mL from all four stock solutions were poured into one beaker in the aforementioned listed order with 0.1 mL of 0.01 M acetylacetone as a stabilizing agent. The final solution, herein referred to as the precursor solution, was left to stir on a magnetic stirrer for further 24 h at 298 K.

Substrates were cut from fluorine doped tin oxide (FTO) coated on silica glass slides of dimensions 5 cm x 2 cm. Substrates were sequentially washed in an ultrasonic bath at 298 K in a 10% Mucasol solution container, distilled water, a different container of distilled water, acetone, and finally in ethanol for 15 min each. Substrates were then placed in storage containers filled with ethanol and stored until deposition with dip-coating.

3.2.2 Dip-coating deposition

A sample was first taken out of storage from an ethanol container and dried with a nitrogen gas purge. Dried substrate surfaces were then placed in a ultraviolet- ozone (UV-O_3) cleaner for 60 min to clean the surface and improve adhesion, while 100 mL precursor solution was poured into an alumina container and placed under the mechanical arm of the dip-coater. The substrate was then attached to the mechanical arm of an in-house dip-

coater seen in fig. 3.2a. The substrate was immersed into the solution, where it rested for 60 s in order to establish equilibrium and finally withdrawn with the same speed as the immersion. The immersion and withdrawal speeds were 0.5 cm min^{-1}, 5.0 cm min^{-1}, 6.0 cm min^{-1}, 18.0 cm min^{-1} or 30.0 cm min^{-1}. The substrate was then carefully removed from the mechanical arm.

After being removed from the mechanical arm of the dip-coater, the deposited sample was placed in an exicator attached to a mechanical pump. Vacuum was introduced to the chamber to promote drying of the solvent for 20 min. Towards the winter season, the ambient temperature dropped lower than 298 K and the substrates were left to dry in a fume hood for 30 min, to avoid crystallization occurring in the film before annealing.

The substrates were then placed in a quartz ship and placed inside a quartz tube. The tube was the placed in a tube furnace and sealed. A flow of 1.0 L min^{-1} argon gas was introduced to the chamber and circulated for 30 min to introduce an inert atmosphere. The temperature was set to a ramp rate of 450 °C h^{-1}, with a set target of 500 °C and a dwell time. A step rate down to 25 °C was set after the dwell time was completed. The dwell time, herein referred to as the annealing time, was 1 h for a single layer deposited. A ring-shaped film was observed after annealing the samples withdrawn at 18 cm min^{-1} and 30 cm min^{-1}. To solve this issue, tape was used to form a square stencil on the substrate surface for deposition by dip-coating. After drying, the Kapton tape was removed and the samples would then be annealed as usual. The use of Kapton tape was maintained for the entirety of the next experiments.
For deposition of a second layer, the method was repeated from placing the sample in a UV-O_3 cleaner to the annealing stage, without any other form of washing or preparation. A fixed withdrawal speed of 30 cm min^{-1} and Kapton tape was used for every deposition, with an annealing time of 1 h or 12 h per layer. The total annealing time for a two-layered sample was therefore 2 h or 24 h.

3.2.3 Angle dependent dip-coating

Angle dependent dip-coating was performed by attaching an additional set piece to the mechanical arm, and measuring the angle of the piece with a protractor prior to attachment. The piece is seen in fig.3.2b. Substrates were attached to the piece by a double-sided scotch tape. Dip angles of substrates θ_s were 60 °, 45°, 30°, 20° or 10°, with a fixed vertical withdrawal speed of 30 cm min^{-1} and Kapton tape. The method was repeated otherwise from placing the sample in a UV-O_3 cleaner to the annealing stage. The annealing time was 1 h for a single layer deposited.
For deposition of a second layer, the method was repeated from placing the sample in a UV-O_3 cleaner to the annealing stage, without any other form of washing or preparation. A fixed vertical withdrawal speed of 30 cm min^{-1}, dip angle of 10° and Kapton

tape was used for every deposition. The annealing time was 0.5 h for the first layer. The annealing times for the second layer were 3 h, 6 h or 12 h. The total annealing time for a two-layered angle dependent sample was therefore 3.5 h, 6.5 h or 12.5 h.

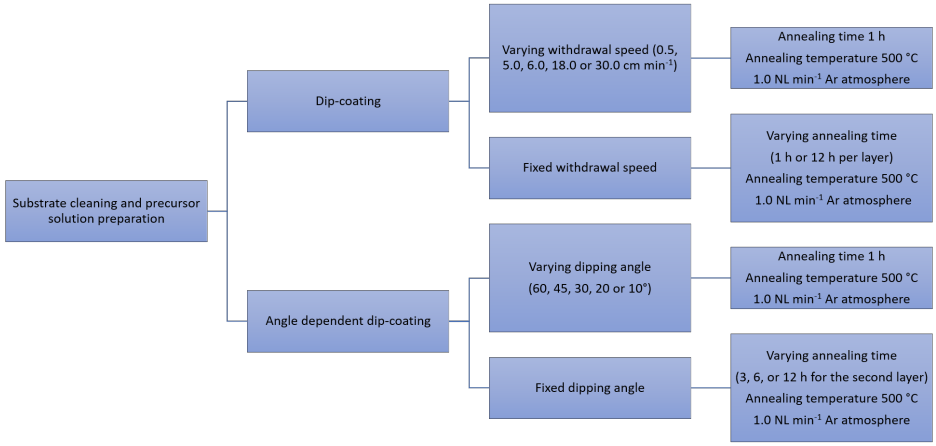

Figure 3.1: A summary of the experimental procedure

3.3 Characterization and instrumentation

Dip-coating was done by an in-house setup with a manual controller that had an accuracy of 0.2 min^{-1}, and with an in-house made aluminium attachment to the mechanical arm permitted the use of angle dependent dip-coating. The in-house setup and aluminium attachment for angle dependent dip-coating can be seen on fig.3.2a and fig.3.2b respectively. Substrate surface preparation was preformed with a Novascan, PSD Pro Series - Digital UV Ozone System. Annealing was performed with Forno Mab, TOL-series Monozone tube furnace with a PXR microcontroller, equipped for argon atmosphere with a glass tube rotameter and range of 0.1-2 NL min^{-1}. XRD measurements were performed with a Rigaku, MiniFlex 600 equipped with a Cu K_α X-ray source (1.5406 Å) and compared with a CZTS diffractogram reference from Nitsche et al.[84] received from the International Centre for Diffraction Data[85] (PDF card no. 00-026-0575). Raman measurements were performed with a Jasco, Ventuno micro-Raman spectrometer equipped with a 633 nm laser and compared with known Raman peaks for a CZTS sample from Trifiletti et al.[63] SEM surface images were performed with a ZEISS, Gemini

500 field equipped for EDXS with a Bruker, QUANTAX XFlash 4000. An accelerating voltage of 5, 15 and 20 kV are used for the in-lens configuration, while an accelerating voltage of 5 kV is used for the asymmetric configuration. An accelerating voltage of 20kV and an aperture of 60 μm was used for surface EDXSmeasurements. The characterization and instruments listed in this paragraph were situated in the Department of Materials Science and Solar Energy Research Center (MIBSOLAR), University of Milano - Bicocca (UNIMIB).

(a)

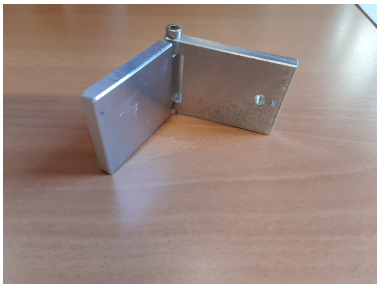

(b)

Figure 3.2: (a) The in-house dip-coater setup. **(b)** The in-house made aluminium piece that could be attached to the mechanical arm and used to perform angle dependent dip-coating.

UV-VIS spectroscopy was performed with an in-house setup containing a Newport, 300 W xenon arc lamp with a Avantes, Avaspec-2048 detector. Additional SEM was performed with a Zeiss, Supra 55VP field emission equipped for EDXS with a Ametek, Octane Pro. For cross section EDXS analysis, an accelerating voltage of 15 kV, an aperture of 60 μm and high current mode was used. Element mapping was performed with a resolution of 516x400 and line scans were performed with a resolution of 0.01μm. Before cross-section SEM and EDXS measurements, samples were carbon sputtered with a Cressington, 208 Carbon coater for 16 s at 4.8 V using graphite rods. Samples were then wrapped in aluminium foil, all to minimize build-up of charge on the surface. Therefore, aluminium and carbon were omitted from the cross-section EDXS measurements. The characterization and instruments listed in this paragraph were situated in the Department of Materials Science and Engineering (IMA) at the Norwegian University of Science and Technology (NTNU).

Chapter 4

Results

4.1 Dip-coating

4.1.1 Withdrawal speed

Raman spectra from samples withdrawn at speeds 0.5 cm min^{-1}, 5.0 cm min^{-1} and 6.0 cm min^{-1} are shown in fig. 4.1. Table 4.1 shows the Raman peaks of possible phases

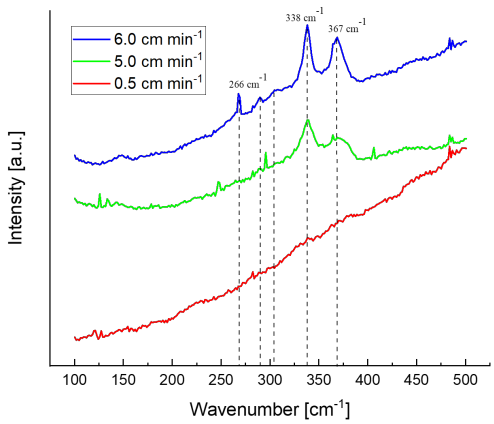

Figure 4.1: Raman spectra from samples withdrawn at 0.5 cm min^{-1}, 5.0 cm min^{-1} and 6.0 cm min^{-1}. Dashed lines are a reference for known Raman peaks in a CZTS sample.

associated with annealed samples.

Table 4.1: Raman peaks of possible phases in annealed samples, reference and excitation lengths used in reference

Phase	Wavenumber [cm^{-1}]	Excitation wavelength [nm]	Reference
CZTS	140, 164, 263, 287, 302, 338, 366	633	[86]
ZnS	216, 352	633	[87]
SnS	163, 189, 220	633	[88]
Sn_2S_3	307	633	[88]
$Cu_{2-x}S$	414, 465, 472	633	[89]
Cubic Cu_2SnS_3	303, 355	488	[90]
Tetragonal Cu_2SnS_3	337, 357	488	[90]

The initial result of withdrawing a sample 0.5 cm min^{-1} showed no distinct peaks. A ten fold increase in withdrawal speed to 5.0 cm min^{-1} showed distinct peaks at 338 cm^{-1} and 366 cm^{-1}, which indicated a CZTS phase[86]. The sample withdrawn at 5.0 cm min^{-1} also displayed smaller peaks appearing at 126 cm^{-1}, 247 cm^{-1}, 296 cm^{-1} and 406 cm^{-1}. A further increase of withdrawal speed showed a larger separation between the two largest peaks, as well as being slightly sharper, at 338 cm^{-1} and 366 cm^{-1}, with a third prominent peak appearing at 266 cm^{-1} further which indicated a CZTS phase present. The peaks at 126 cm^{-1}, 247 cm^{-1}, 296 cm^{-1} and 406 cm^{-1} did not appear in the spectrum of the sample withdrawn at 6.0 cm min^{-1}. Minor peaks appeared in the Raman spectra for the sample withdrawn at 5.0 cm min^{-1} and did not match with any reference data for possible secondary phases seen in table. 4.1. The peaks at 296 cm^{-1} and 406 cm^{-1} could have experienced a bathochromic shift, which would implicate the presence of Sn_2S_3 and $Cu_{2-x}S$ respectively. All Raman spectra for the samples with varied withdrawal speed also showed small and sharp peaks around the 480-490 cm^{-1} and may also have exhibited a bathochromic shift, which indicated the presence of $Cu_{2-x}S$. As the withdrawal speed increased from 0.5 to 5.0 cm min^{-1}, a noticeable change in darker color was also observed for the deposited film.

Raman spectra of the deposited ring-shaped edge films and its centers for withdrawal speeds 18.0 cm min^{-1} and 30.0 cm min^{-1} are seen in fig. 4.2a and fig. 4.2b, respectively. For both of the speeds 18.0 cm min^{-1} and 30.0 cm min^{-1}, the center and the ring displayed two large peaks at 338 cm^{-1} and 366 cm^{-1} which indicated the presence of CZTS phases, and small peaks in the 480-490 cm^{-1} range possibly exhibited by $Cu_{2-X}S$ in the sample. A small peak appeared in fig. 4.2b at 183 cm^{-1} could be exhibiting a bathochromic shift, thus indicating the presence of SnS. The difference between the Raman spectra for the ring-shaped edge compared to its center, appeared to be larger for the sample withdrawn at 18.0 cm min^{-1} as there was a clearer baseline correction for the former site. This would entail that CZTS phases were lost in the center area for the sample withdrawn at 18 cm min^{-1}. The baseline corrections in both Raman spectra were accompanied by a stronger sample absorption and therefore implicated a thicker sample layer, as FTO has been reported to exhibiting weak but increasing absorption from the low 100 cm^{-1} range until around 500 cm^{-1}.[91]

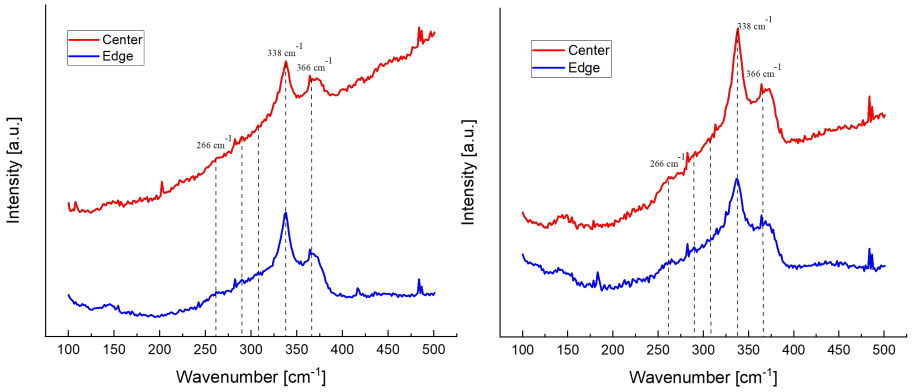

Figure 4.2: **(a)**Raman spectrum from a sample withdrawn at 18.0 cm min^{-1}. **(b)** Raman spectrum from a sample withdrawn at 30.0 cm min^{-1}. Dashed lines in both spectra are a reference for known Raman peaks in a CZTS sample.

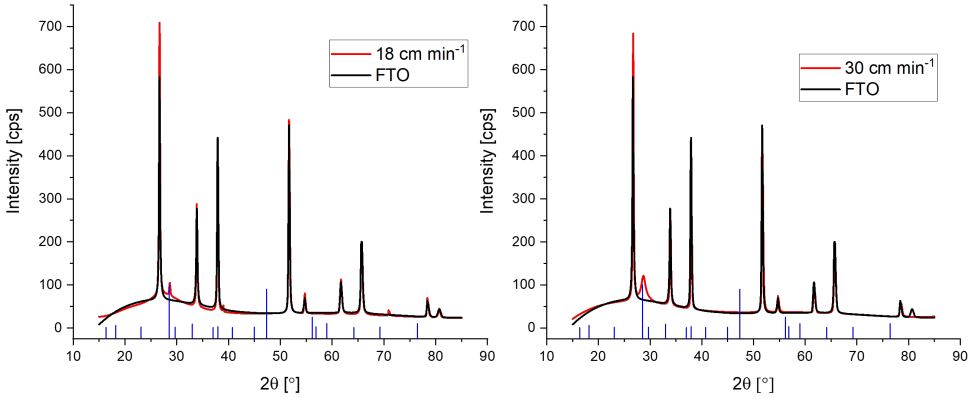

(a) **(b)**

Figure 4.3: **(a)** X-ray diffractogram of a sample withdrawn at 18.0 cm min^{-1} including a clean FTO substrate. **(b)** X-ray diffractogram of a sample withdrawn at 30.0 cm min^{-1} including a clean FTO substrate. Solid blue lines for known XRD peaks of CZTS (PDF card no. 00-026-0575)

X-ray diffractograms for samples with withdrawal speeds of 18.0 cm min^{-1} and 30.0 cm min^{-1} using Kapton are seen in fig. 4.3a and fig. 4.3b respectively, and include an analyzed clean FTO sample. Both diffractograms showed a small peak around 28.7 ° exhibited a minor shift from the reference CZTS standard at 28.5°, but indicated that there might be CZTS phases present. The peak was slightly larger for the sample withdrawn at 30.0 cm min^{-1} compared to the sample withdrawn at 18.0 cm min^{-1} which indicated a higher degree of CZTS phases. The latter sample also displayed a minor peak at 71.1 ° which was not present in the former. This peak could have been attributed to CZTS phases as well ZnS or Cu_2SnS_3.

UV-VIS spectra for samples with withdrawal speeds of 18.0 cm min^{-1} and 30.0 cm min^{-1} using Kapton are shown in fig. 4.4a and fig. 4.4b, respectively.

The UV-VIS spectrum taken for the sample withdrawn at 18.0 cm min^{-1} exhibited more noise in the spectra compared to the sample withdrawn at 30.0 cm min^{-1}, especially towards the edges of the recorded range. The latter also has a more distinct change in absorbance in the 600-800 nm range. A higher absorbance in this range indicated a higher absorbance within the largest section of terrestrial radiance as seen in fig. 2.2.
Surface SEM images at low resolution of samples with withdrawal speeds 18.0 cm min^{-1} and 30.0 cm min^{-1} were taken and are seen in fig. 4.5a and fig. 4.6a, respectively. Small crystallites were observed on the surfaces of both samples. On the surface of the sample withdrawn at 18.0 cm min^{-1}, the crystallites generally appeared to be smaller than the

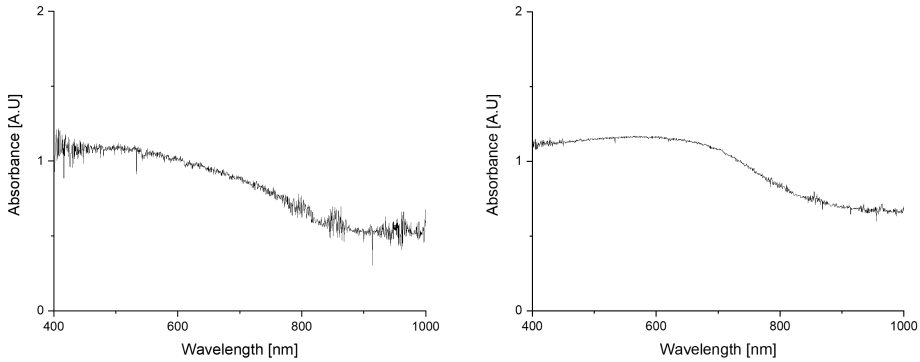

(a) **(b)**

Figure 4.4: **(a)** UV-VIS spectra of a sample withdrawn at 18.0 cm min^{-1}. **(b)** UV-VIS spectra of a sample withdrawn at 30.0 cm min^{-1}.

crystallites on the surface of the sample withdrawn at 30.0 cm min^{-1}. The crystallites on the surface are seen in a higher resolution for samples withdrawn at 18.0 cm min^{-1} and 30.0 cm min^{-1} in fig. 4.5b and 4.6b respectively.

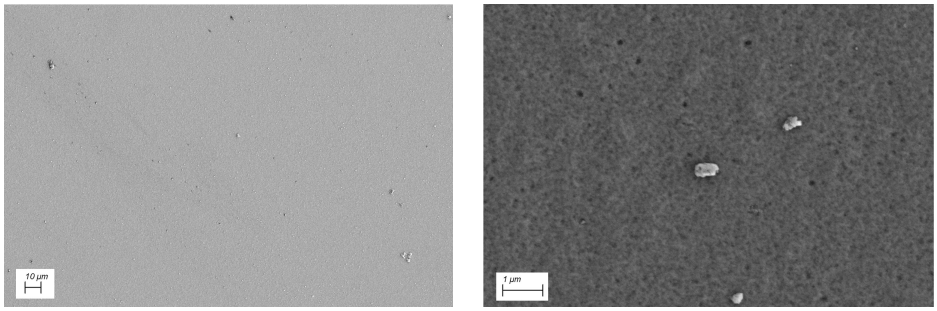

(a) **(b)**

Figure 4.5: Surface SEM images of a sample withdrawn at 18.0 cm min^{-1} at **(a)** low resolution and **(b)** high resolution.

The crystallites on the surface SEM images could have been secondary phases present or possibly polymorphs of CZTS.
Surface SEM image of crystallites on the sample withdrawn at 30.0 cm min^{-1} and the corresponding surface EDXS element mapping are shown in fig. 4.7a and fig. 4.7b. The surface EDXS spectra for the former are shown in fig. 4.7c and fig. 4.7d; marked

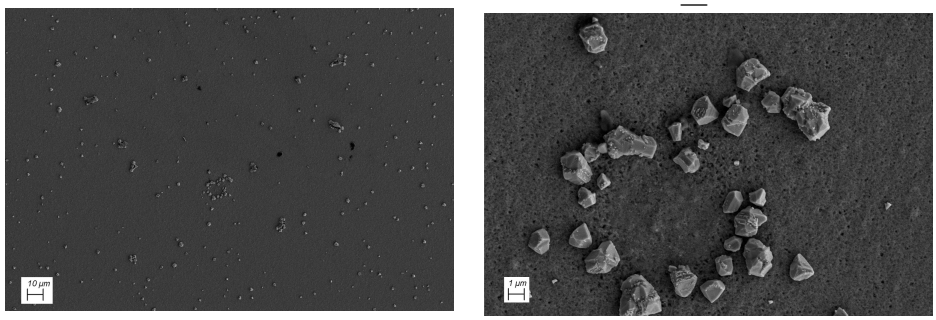

(a) **(b)**

Figure 4.6: Surface SEM images of a sample withdrawn at 30.0 cm min^{-1} at **(a)** low resolution and **(b)** high resolution.

with a green circle and a yellow circle respectively. Surface EDXS element mapping in fig. 4.7b showed that the crystallites were rich in copper and sulfur, and perhaps zinc, compared to the background. The crystallites were not rich in tin compared to the background. The tin signal in the crystallite could however have been influenced by the contribution of the FTO substrate. These observations were also confirmed in fig. 4.7c with an intense Sn L_α peak, and in fig. 4.7d with an intense S K_α peak, and more intense Cu K_α and Zn K_α peaks than in fig. 4.7c.

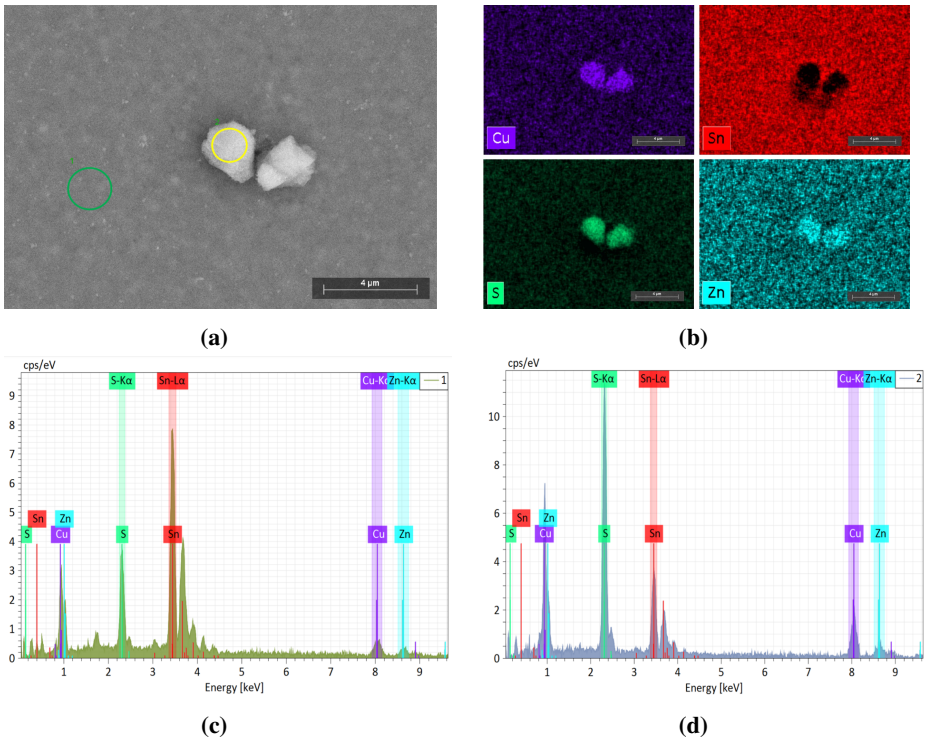

Figure 4.7: **(a)** Surface SEM image of crystallites on a sample withdrawn at 30.0 cm min^{-1} and **(b)** corresponding surface EDXS element mapping. **(c)** Surface EDXS spectra of area 1, marked with a green circle in fig.4.7a. **(d)** Surface EDXS spectra of area 2, marked with a yellow circle in fig. 4.7a.

4.1.2 Annealing time with fixed withdrawal speed

Raman spectra for each layer in two-layered samples with fixed withdrawal speed, and annealing time of 1 h or 12 h per layer are shown in fig. 4.8a and fig. 4.8b respectively. Each layer of the sample annealed 1 h per layer showed two large peaks at 338 cm^{-1} and 366 cm^{-1}, indicative of a CZTS phase. After annealing 2 layers, smaller peaks at 263 cm^{-1}, 287 cm^{-1} and 302 cm^{-1} appeared, which were also Raman peaks associated with CZTS. The same peaks appeared to be slightly shifted towards higher wavenumbers after annealing the first layer. Each layer of the sample annealed 12 h per layer showed one clear peak at 338 cm^{-1}, but only the first annealed layer showed distinct peaks 367 cm^{-1}; both peaks would have indicated the presence of CZTS in the sample. The first annealed layer also had a clear baseline correction compared to the two annealed layers.

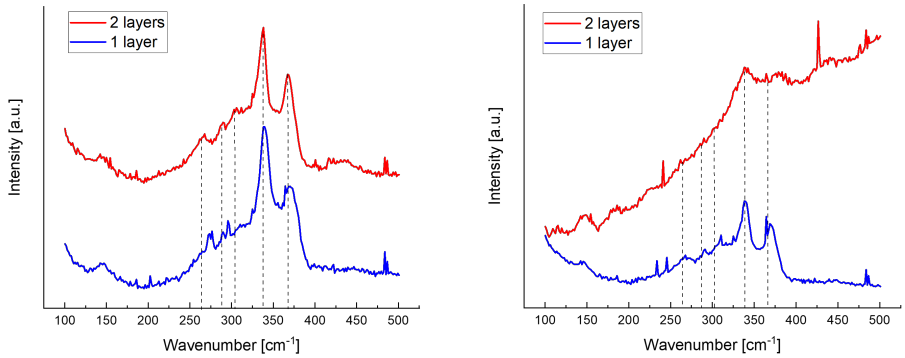

Figure 4.8: (a) Raman spectra of each layer for a two-layered sample annealed 1 h per layer. **(b)** Raman spectra of each layer for a two-layered sample annealed 12 h per layer. Dashed lines in both spectra are a reference for known Raman peaks in a CZTS sample.

The two annealed layers showed sharp peaks at 241 cm^{-1} and 427 cm^{-1} which did not correspond to any known Raman peaks for phases associated with the samples. Small, sharp peaks are also observed for both spectra in the 480-490 cm^{-1} range, which possibly could have indicated the presence of $Cu_{2-X}S$. Both spectra for the first layer, shown in blue, also displayed a split peak.
X-ray diffractograms of two-layered samples annealed 1 h and 12 h for each layer are shown in fig. 4.9a and fig. 4.9b respectively. The largest peak measured for the two-layered sample annealed 1 h each layer appeared at 28.7° in fig. 4.9a and at 28.5° in fig. 4.9b and both indicated the presence of CZTS. The second largest peak for the former sample appeared at 47.6°, while the same peak hardly appeared in the latter sample. The two-layered sample annealed 1 h each layer had its third largest peak at 56.5° and the same peak did not appear in the two-layered sample annealed 12 h each layer. Both peaks at 47.6° and 56.5° indicated the presence of CZTS phases. The minor peak at 38.9° in both fig.4.9a and fig.4.9b, and the minor peaks in the latter at 70.9°, 72.9° and 83.2° could have belonged to secondary phases present in the sample. The small peak at 70.9° could have belonged to ZnS, Cu_2SnS_3 or CZTS phases in the sample. The peak at 83.2° could have been evidence of a SnS_2 phase in the sample.

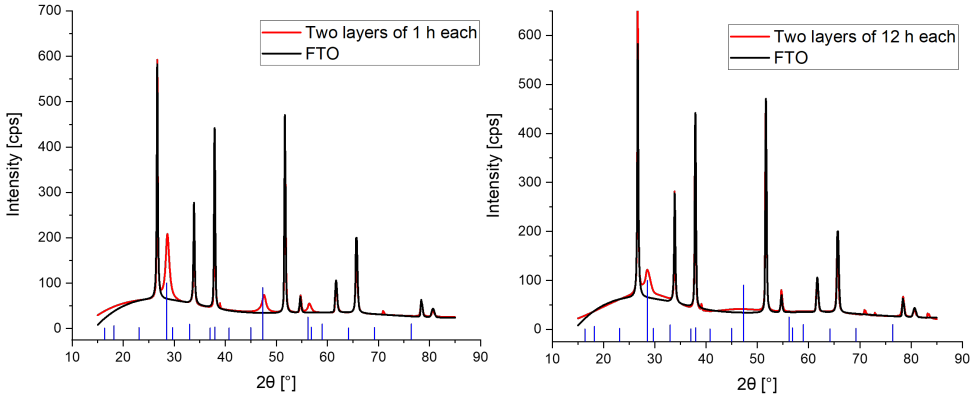

(a) **(b)**

Figure 4.9: **(a)** X-ray diffractogram of a two-layered sample with fixed withdrawal speed and annealed 1 h for each layer, including a clean FTO substrate. **(b)** X-ray diffractogram of a two-layered sample with fixed withdrawal speed and annealed 12 h for each layer, including a clean FTO substrate. Solid blue lines for known XRD peaks of CZTS (PDF card no. 00-026-0575)

Table 4.2 shows angle of peaks not associated with FTO and their the full width at half-maximum (FHWM) for two-layered samples with fixed withdrawal speed and annealing time of 1h or 12 h each layer. The FWHM for the largest peak in fig.4.9a is smaller than the FWHM of the largest peak in fig.4.9b and if both peaks correspond to CZTS, then that would indicate a smaller grain size in the latter.

Table 4.2: angle of peaks not associated with FTO and their FHWM for two-layered samples with fixed withdrawal speed and annealing time of 1h or 12 h each layer. The FWHM values were calculated using built-in software.

Annealed 1 h each layer	
2θ [°]	FWHM [°]
28.66	0.84
38.98	0.08
56.46	0.75
70.94	0.23

Annealed 12 h each layer	
2θ [°]	FWHM [°]
28.52	1.13
39.10	0.19
70.92	0.20
72.94	0.10
83.24	0.25

UV-VIS spectra of two-layered samples annealed 1 h and 12 for each layer are shown in fig. 4.10a and fig. 4.10b respectively.

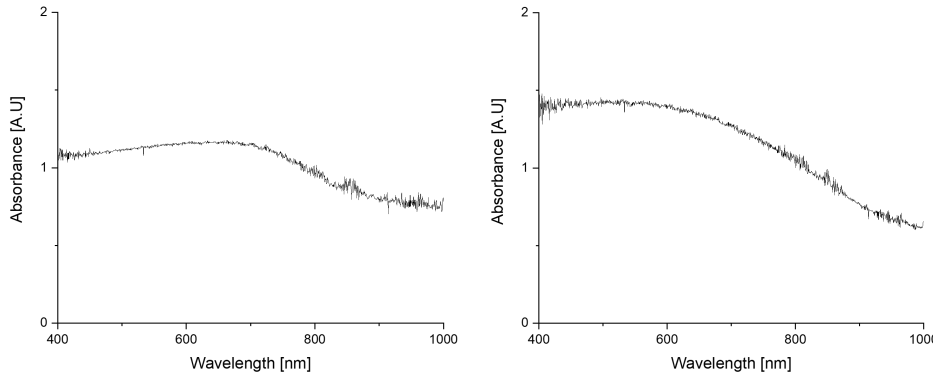

(a) **(b)**

Figure 4.10: **(a)** UV-VIS spectra of a two-layered sample with fixed withdrawal speed and annealed 1 h for each layer. **(b)** UV-VIS spectra of a two-layered sample with fixed withdrawal speed and annealed 12 h for each layer.

Both spectra for the two-layered samples showed absorption in the 600-800 nm range. The UV-VIS spectra for the two-layered sample annealed 12 h each layer displayed also further distinct absorption towards 900 nm. The onset of absorption appeared to occur for a higher wavelength, around 650 nm, in comparison to the two-layered sample annealed 1 h each layer. Both UV-VIS spectra exhibited an absorption within the largest portion of terrestrial radiance as seen in fig.2.2
Surface SEM images of two-layered sample with fixed withdrawal speed and annealed 1 h for each layer, seen at low and high resolution are shown in fig. 4.11a and fig. 4.11b respectively. The surface SEM image at high resolution in fig.4.11b showed little to no porosity and small crystallites on the surface. These crystallites could have been different polymorphs of CZTS or secondary phases. Surface SEM images of two-layered sample with fixed withdrawal speed and annealed 12 h for each layer, seen at low and high resolution are shown in fig. 4.12a and fig. 4.12b. The surface SEM image at high resolution seen in fig. 4.12b showed a more distinct porosity on the nanoscale, while the lower resolution showed darker spots, which possibly could have indicated different phases on the surface. There appears to be a trade-off between crystallites on the surface at shorter annealing times, and higher porosity at longer annealing times.

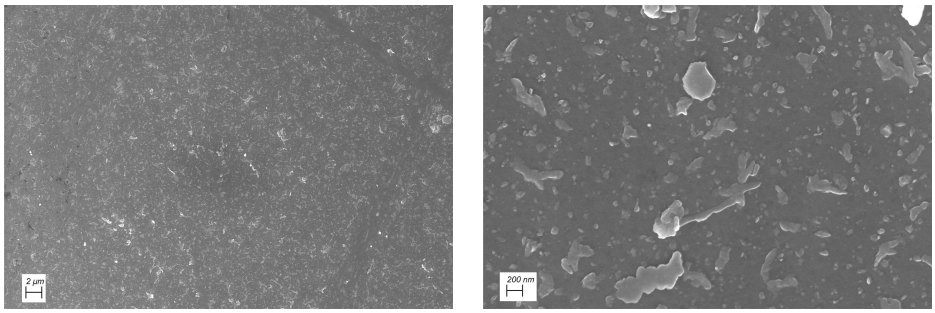

(a) **(b)**

Figure 4.11: Surface SEM images of a two-layered sample with fixed withdrawal speed and annealed 1 h for each layer. **(a)** low resolution and **(b)** high resolution.

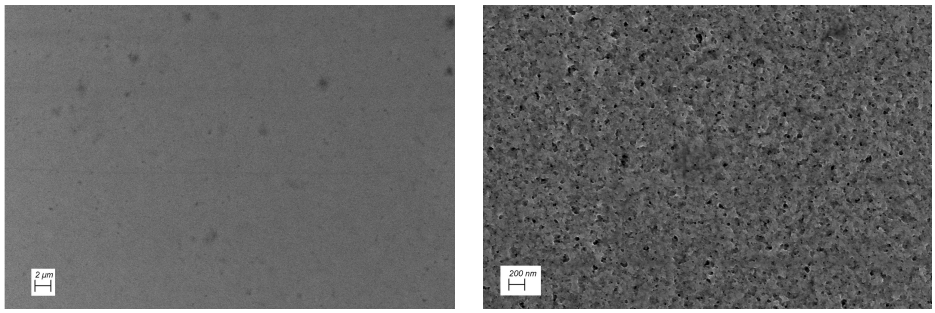

(a) **(b)**

Figure 4.12: Surface SEM images of a two-layered sample with fixed withdrawal speed and annealed 12 h for each layer. **(a)** low resolution and **(b)** high resolution.

The cross-section SEM image, EDXS line scan and element mapping for the two-layered sample with fixed withdrawal speed and annealed for 1 h each layer can be seen in fig. 4.13a, fig. 4.13b and fig.4.13c respectively. The cross-section SEM image in fig. 4.13a showed a measured thickness of around 600 nm, and the EDXS line scan in fig. 4.13b showed a measured thickness of around 710 nm and 850 nm for the intersections of the sulfur signal with the tin and oxygen signal respectively.
The EDXS sulfur map in fig. 4.13c showed a clear separation between the two-layered sample bulk and the substrate, with copper and some zinc present in the two-layered sample. Oxygen was also present in the two-layered sample which indicated a degree of diffusion from the substrate.
The cross-section SEM image, EDXS line scan and element mapping for the two-layered

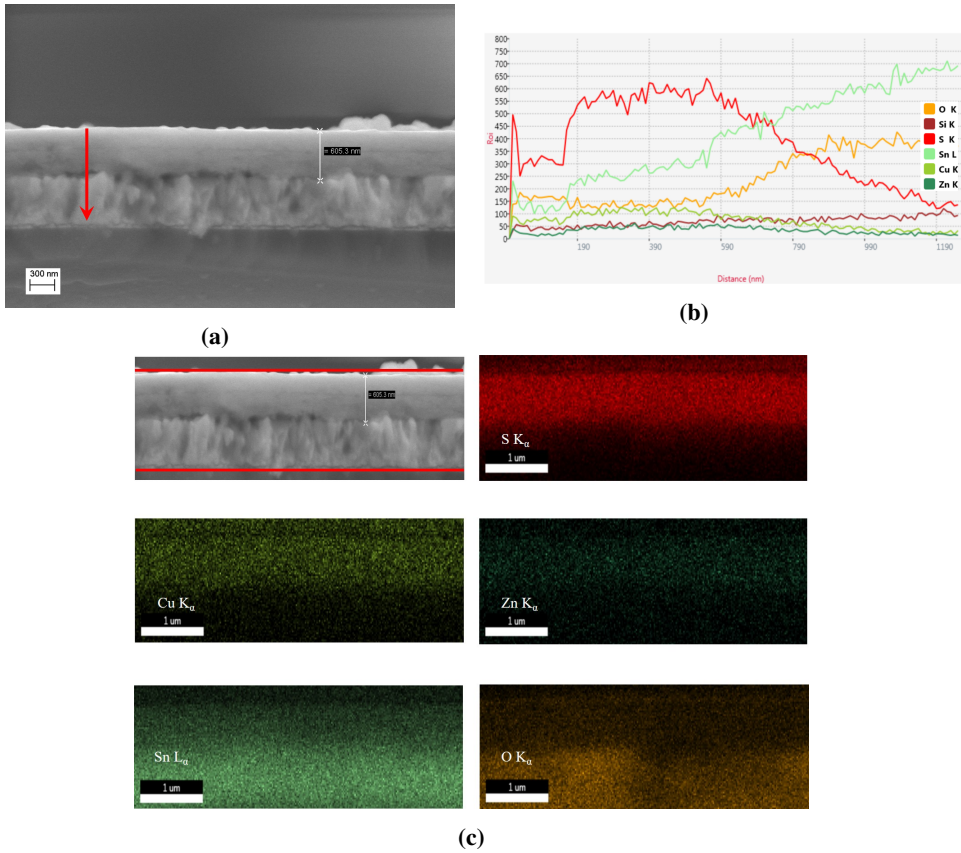

Figure 4.13: **(a)** Cross-section SEM image of a two-layered sample with fixed withdrawal speed and annealed 1 h for each layer. The red line marks line scan position. **(b)** Cross-section EDXS line scan oriented from surface towards the substrate and **(c)** cross-section EDXS mapping of elements . Red lines in the top right mark the area of mapping.

sample with fixed withdrawal speed and annealed 12 h for each layer are shown in fig. 4.14a, fig. 4.14b and fig.4.14crespectively. The cross-section SEM image in fig. 4.14a showed a measured thickness of around 660 nm, and the EDXS line scan in fig. 4.14b showed a measured thickness of around 850 nm for the intersections of the sulfur signal with the tin and oxygen signal. The EDXS sulfur map in fig. 4.14c showed a clear separation between the two-layered sample bulk and the substrate, with copper and some zinc present in the two-layered sample. Sodium, and some oxygen, was also highly present in the two-layered sample which indicated a large degree of diffusion from the

substrate. Table 4.3 shows the measured thicknesses of two-layered samples with fixed

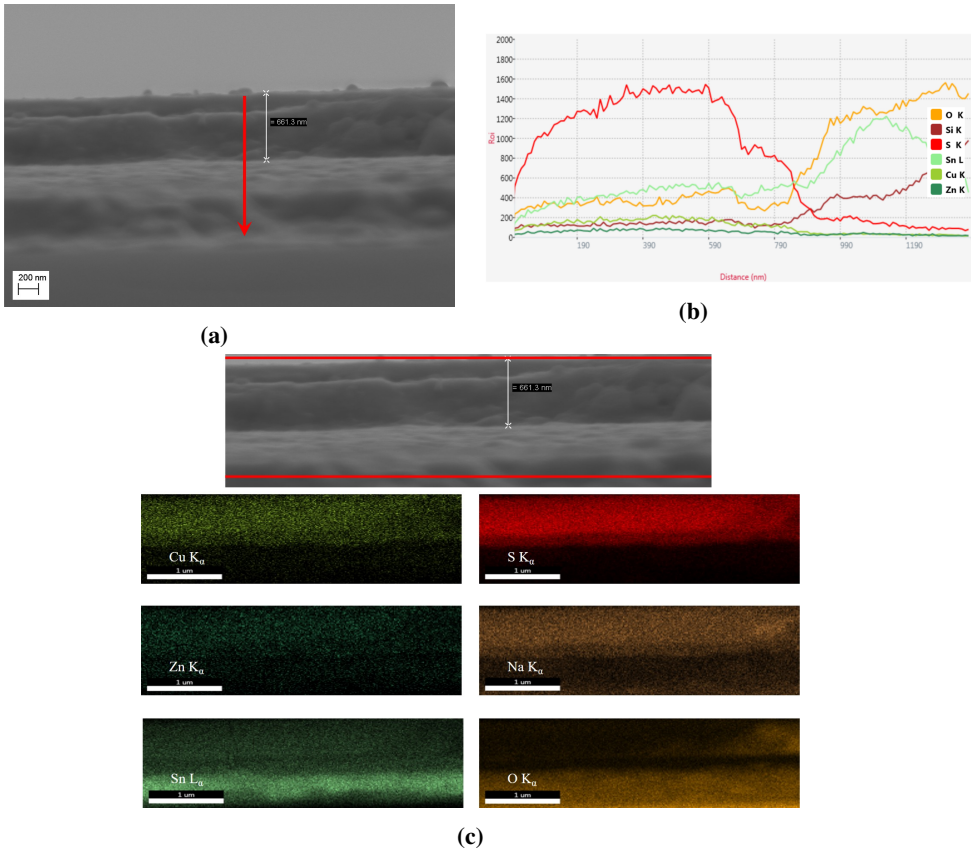

Figure 4.14: **(a)** Cross-section SEM image of a two-layered sample with fixed withdrawal speed and annealed 12 h for each layer. The red line marks line scan position. **(b)** Cross-section EDXS line scan oriented from surface towards the substrate and **(c)** cross-section EDXS mapping of elements. Red lines in the top image illustrates the area of mapping.

withdrawal speed and an annealing time of 1 h or 12 h for each layer using different sources to calculate and average thickness value. Considering the average thickness values in table 4.3, a longer annealing time for each layer appeared to result in a thicker two-layered sample.

Table 4.3: Measured thicknesses for two-layered samples with fixed withdrawal speed and annealed for 1 h or 12 h each layer. The sources of data were cross-sectional SEM images and EDXS line scans, where the latter applied the distance to the intersection between the sulfur signal and the tin or oxygen signal. All measurements and averages are rounded to nearest 10 nm.

	Measured thickness [nm]			
Annealing time for each layer [h]	Cross-section SEM	Cross-section EDXS line scan using Sn signal	Cross-section EDXS line scan using O signal	Average [nm]
1	600	710	850	720
12	660	850	850	790

Tauc plots calculated for two-layered samples with fixed withdrawal speed and annealed for 1 h and 12 h each layer are shown in fig. 4.15a and fig. 4.15b respectively. The estimated bandgap values for the two-layered samples with fixed withdrawal speeds and annealed for 1 h or 12 h each layer were 1.28 eV, and 1.31 eV respectively. They were both below the expected bandgap value of CZTS around 1.5 eV.

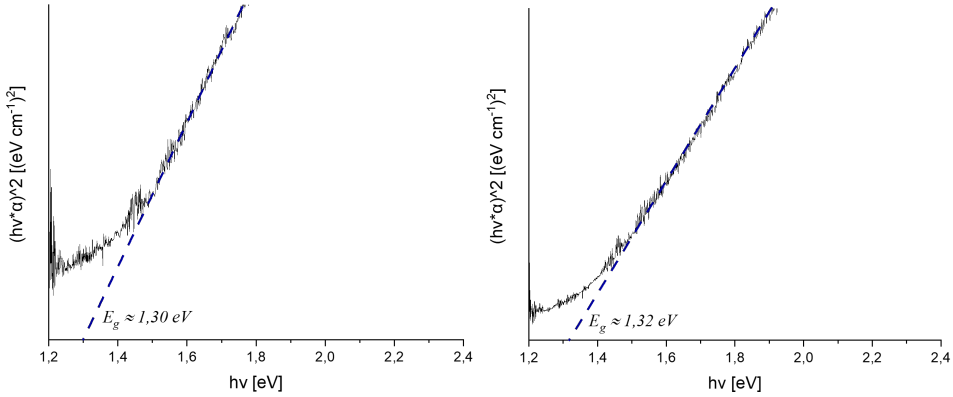

(a) **(b)**

Figure 4.15: Tauc plots for two-layered samples with fixed withdrawal speed annealed **(a)** 1 h for each layer and **(b)** 12 h each layer. Calculations were done with average thickness values in table 4.3

4.2 Angle dependent dip-coating

4.2.1 Dip angle

Cross-sectional SEM image, EDXS line scan and element mapping of a sample with dip angle of 60° can be seen in fig. 4.16a, fig. 4.16b and fig. 4.16c respectively. The cross-

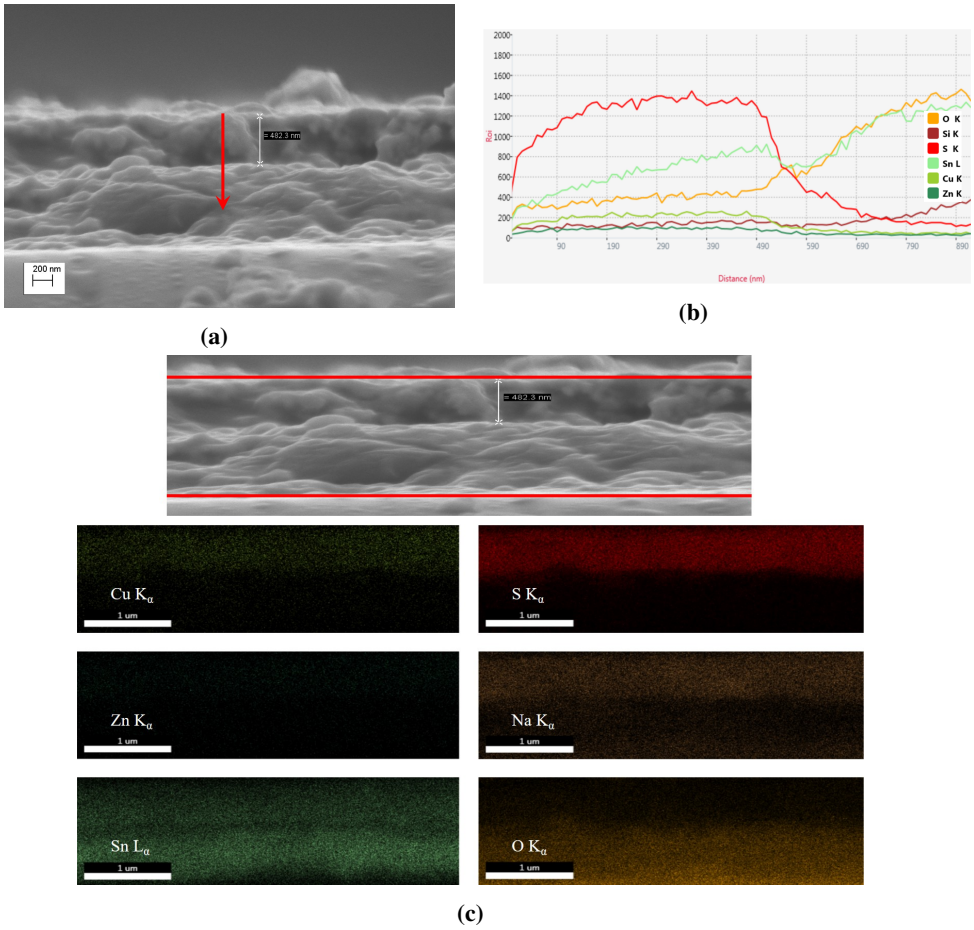

Figure 4.16: **(a)** Cross-section SEM image of sample with a dip angle of 60 °. The red vertical line marks line scan position. **(b)** Cross-section EDXS line scan oriented from surface towards the substrate and **(c)** EDXS element mapping. Red horizontal lines mark the scanning area.

section SEM image in fig. 4.16a showed a measured thickness of around 480 nm, and the

EDXS line scan in fig. 4.16b showed a measured thickness of around 550 nm and 560 nm for the intersections of the sulfur signal with the tin and oxygen signal respectively. The EDXS sulfur map in fig. 4.16c showed a clear separation between the two layers with little to no copper and zinc. Sodium was also present in the sample which indicated a degree of diffusion from the substrate.
Cross-sectional SEM image, EDXS line scans and element mapping of a sample with dip angle of 45° can be seen in fig. 4.17a, fig. 4.17b and fig. 4.17c respectively. The cross-section SEM image in fig. 4.17a showed a measured thickness of around 410 nm, and the EDXS line scan in fig. 4.17b showed a measured thickness of around 420 nm and 460 nm for the intersections of the sulfur signal with the tin and oxygen signal respectively. The EDXS sulfur map in fig. 4.17c showed a clear separation between the two layers, with little to no copper and zinc present in the sample.

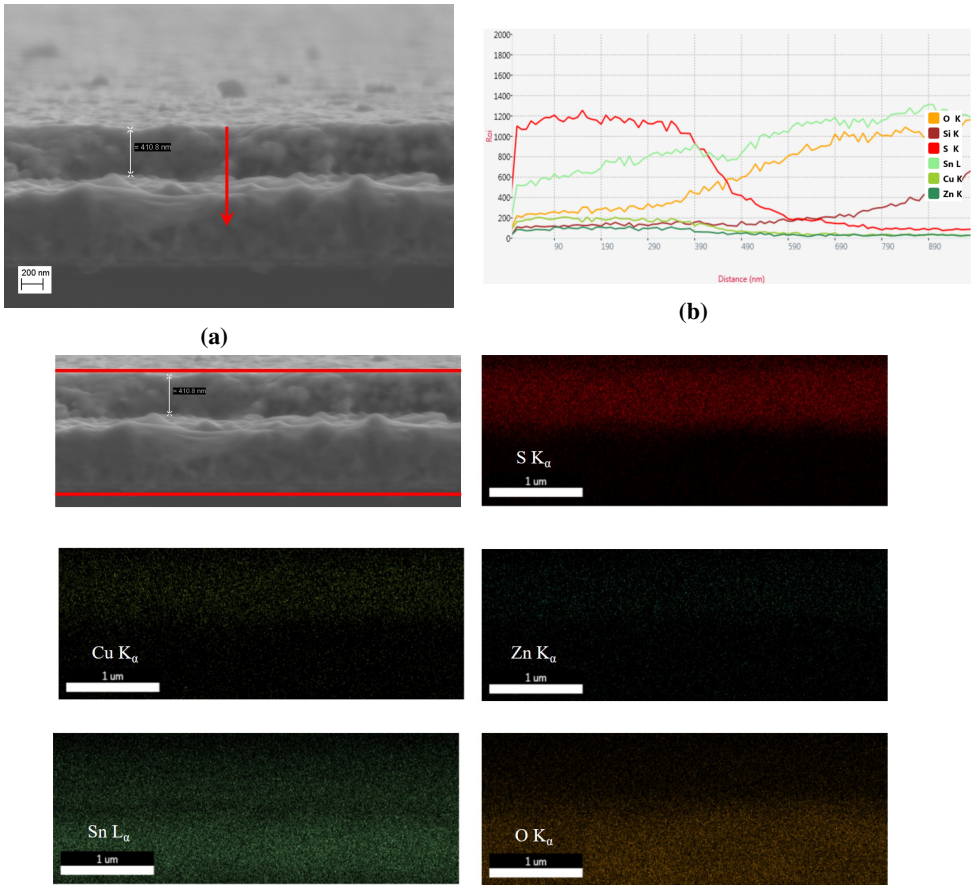

Figure 4.17: **(a)** Cross-section SEM image of sample with a dip angle of 45 °. The red vertical line marks line scan position. **(b)** Cross-section EDXS line scan oriented from surface towards the substrate and **(c)** EDXS element mapping. Red horizontal lines mark the scanning area.

Cross-sectional SEM image, EDXS line scan and element mapping of a sample with dip angle of 30° can be seen in fig. 4.18a, fig. 4.18b and fig. 4.18c respectively. The cross-section SEM image in fig. 4.18a could not show a possible thickness of the sample as the sample and the substrate had the same contrast. The EDXS line scan in fig. 4.18b could not indicate a thickness either as the sulfur signal was continuously lower than the tin signal and oxygen signal. The sample was likely too thin to measure with the two aforementioned methods. The EDXS sulfur map in fig. 4.18c showed a small layer

at the very top of the substrate including very little copper and sodium. Zinc was also not seen clearly in the measured area. The oxygen signal made the dimension of the substrate clearer to distinguish.

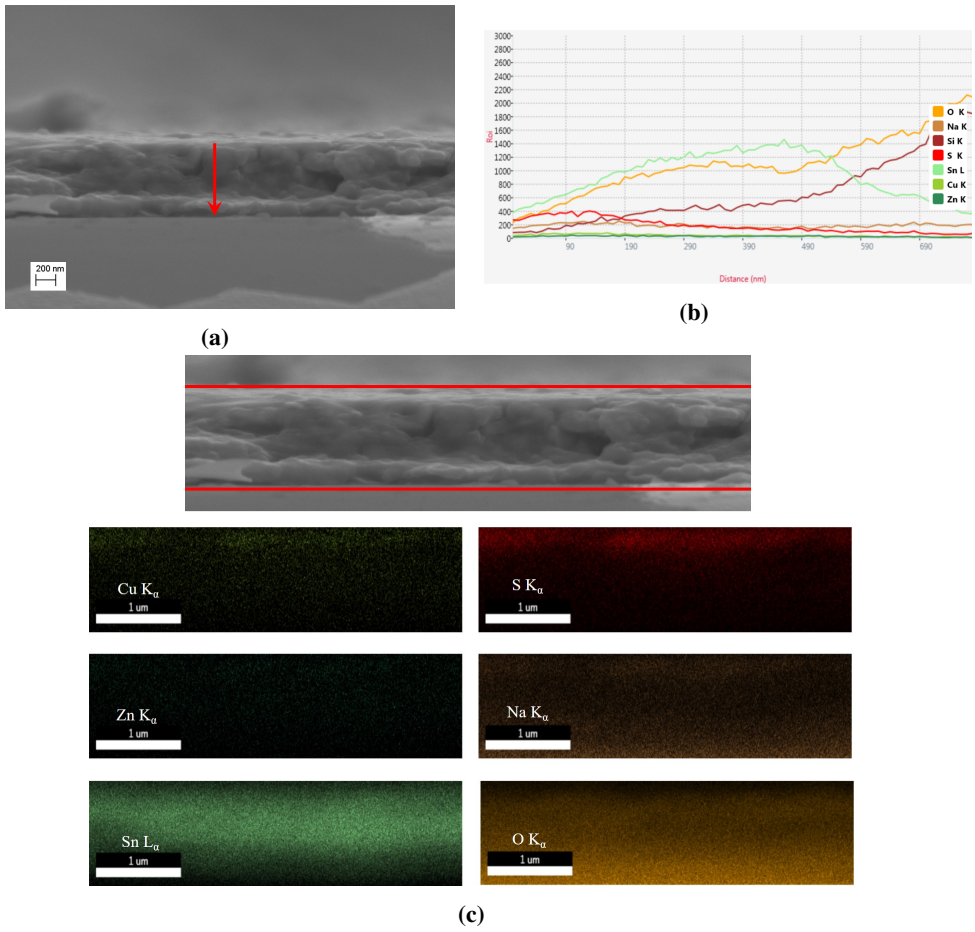

Figure 4.18: **(a)** Cross-section SEM image of sample with a dip angle of 30 °. The red vertical line marks line scan position. **(b)** Cross-section EDXS line scan oriented from surface towards the substrate and **(c)** EDXS element mapping. Red horizontal lines mark the scanning area.

Cross-sectional SEM image, EDXS line scan and element mapping of a sample with dip angle of 20° can be seen in fig. 4.19a, fig. 4.19b and fig. 4.19c respectively. The cross-section SEM image in fig. 4.19a showed a measured thickness of around 400 nm, and the EDXS line scan in fig. 4.19b showed a measured thickness of around 270 nm and 320

nm for the intersections of the sulfur signal with the tin and oxygen signal respectively. The EDXS sulfur map in fig. 4.19c showed a clear separation between the two layers, with little to no copper and zinc present in the sample. Sodium was also present in the sample which indicated a degree of diffusion from the substrate.

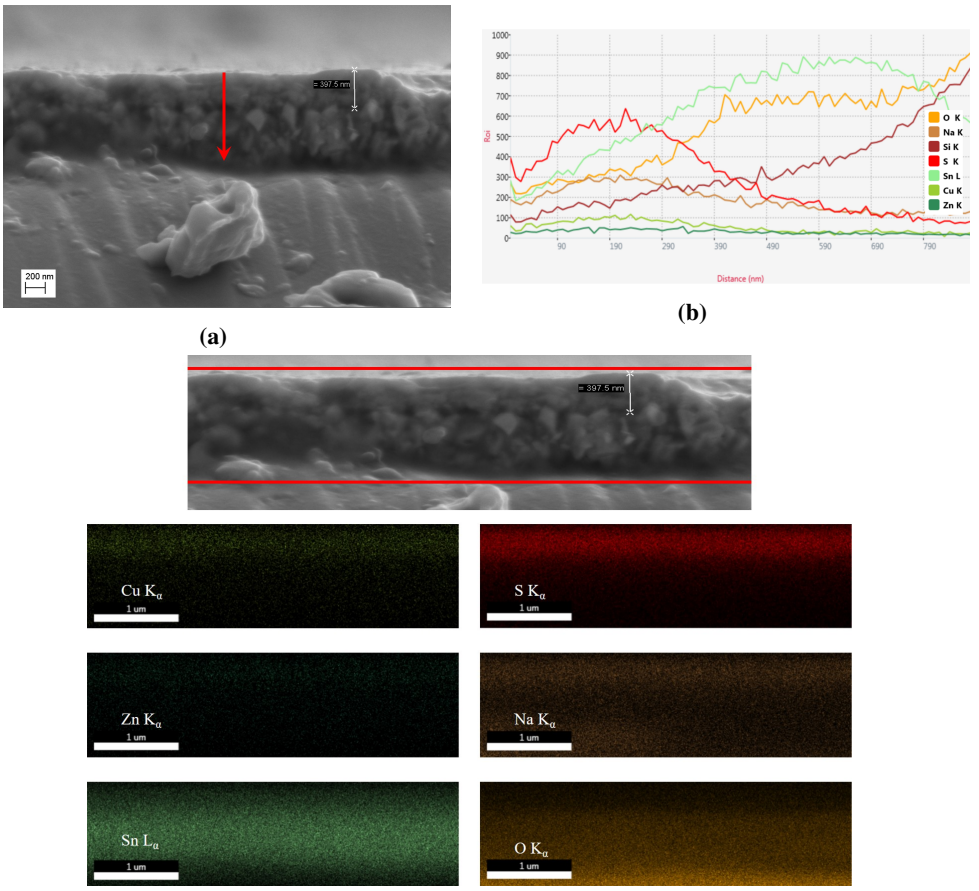

Figure 4.19: **(a)** Cross-section SEM image of sample with a dip angle of 20 °. The red vertical line marks line scan position. **(b)** Cross-section EDXS line scan oriented from surface towards the substrate and **(c)** EDXS element mapping. Red horizontal lines mark the scanning area.

Cross-sectional SEM image, EDXS line scan and element mapping of a sample with dip angle of 10° can be seen in fig. 4.20a, fig. 4.20b and fig. 4.20c respectively. The cross-section SEM image in fig. 4.20a showed a measured thickness of around 560 nm, and the

EDXS line scan in fig. 4.20b showed a measured thickness of around 470 nm and 510 nm for the intersections of the sulfur signal with the tin and oxygen signal respectively. The EDXS sulfur map in fig. 4.20c showed a clear separation between the two layers, with little to no copper and zinc present in the sample. Sodium was also present in the sample which indicaed a degree of diffusion from the substrate.

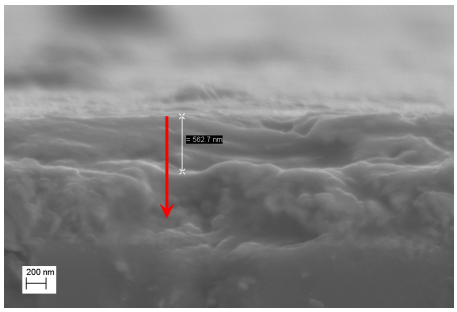

(a)

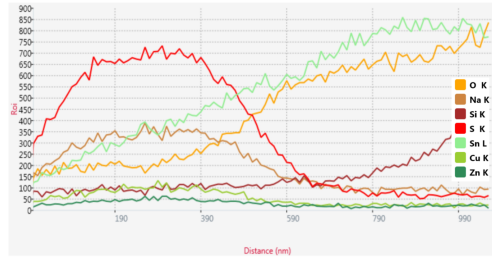

(b)

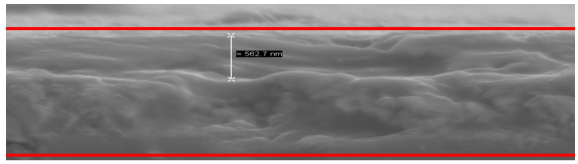

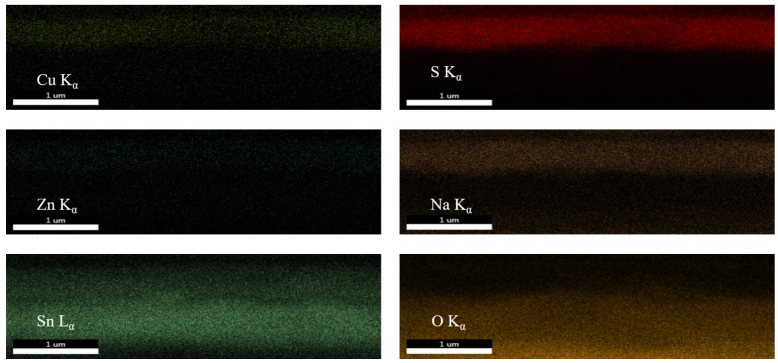

(c)

Figure 4.20: **(a)** Cross-section SEM image of sample with a dip angle of 10 °. The red vertical line marks line scan position. **(b)** Cross-section EDXS line scan oriented from surface towards the substrate and **(c)** EDXS element mapping. Red horizontal lines mark the scanning area

Table 4.4 shows the the measured thicknesses of samples with fixed withdrawal speed and dipped at 60 °, 45°, 30°, 20° or 10° using different sources to calculate an average thickness value.

Table 4.4: Measured thicknesses for samples with fixed withdrawal speed and dip angles of 60 °, 45°, 30°, 20° or 10°. The sources of data were cross-sectional SEM images and EDXS line scans, where the latter applied the distance to the intersection between the sulfur signal and the tin or oxygen signal. All measurements and averages are rounded to nearest 10 nm.

	Measured thickness [nm]			
Dip angle [°]	Cross-section SEM	Cross-section EDXS line scan using Sn signal	Cross-section EDXS line scan using O signal	Average [nm]
60	480	550	560	530
45	410	420	460	430
30	-	-	-	-
20	400	270	320	330
10	560	470	510	510

Based on the average sample thickness values, a decreased angle from 60° to 45° resulted in a decreased sample thickness, and possibly reached a minimum around 30°. The trend was an increase in sample thickness by a further decreased angle to 20° and 10°.

4.2.2 Annealing time with fixed dip angle

Raman spectra for two-layered samples with fixed dip angle and annealing time of 3 h, 6 h and 12 h for the second layer are shown in fig.4.21a, fig.4.21b and fig.4.21c respectively. All three spectra exhibited the two largest peaks expected for CZTS at 338 cm^{-1} and 367 cm^{-1} which indicated the presence of CZTS in the two-layered samples. However, three peaks expected for a CZTS sample at 263 cm^{-1}, 287 cm^{-1} and 302 cm^{-1}

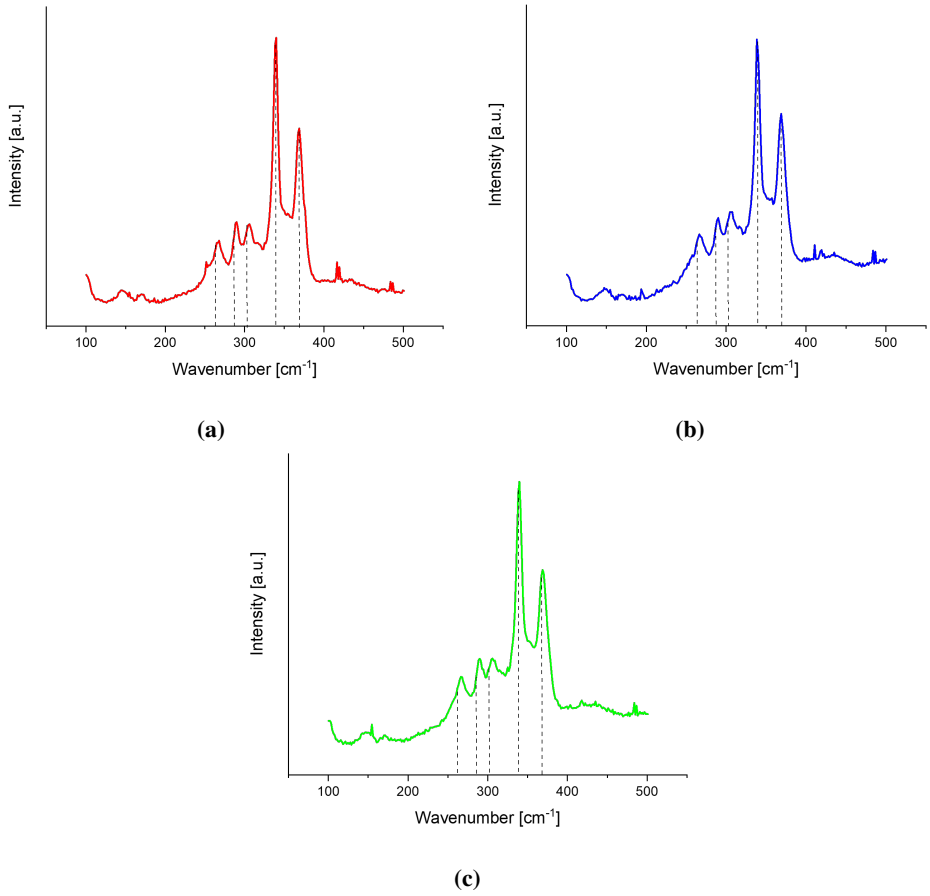

Figure 4.21: Raman spectra for two-layered samples with fixed dip angle and annealed **(a)** 3 h for the second layer, **(b)** 6 h for the second layer and **(c)** 12 h for the second layer. Dashed lines in all spectra are a reference for known Raman peaks in a CZTS sample.

were shifted towards a higher wavenumber in all three spectra but still appeared to belong

to CZTS phases in the sample. All three spectra exhibited small, broad peaks centered around 140 cm^{-1} and 160 cm^{-1} which further indicated the presence of CZTS phases. Sharp peaks in the 480-490 cm^{-1} and small, sharp peaks in the 415-420 cm^{-1} range could have indicated the presence of $Cu_{2-X}S$ phases in the sample. X-ray diffractograms for two-layered samples with fixed dip angle and annealing time of 3 h, 6 h and 12 h for the second layer are shown in fig.4.22a, fig.4.22b and fig.4.22c respectively.

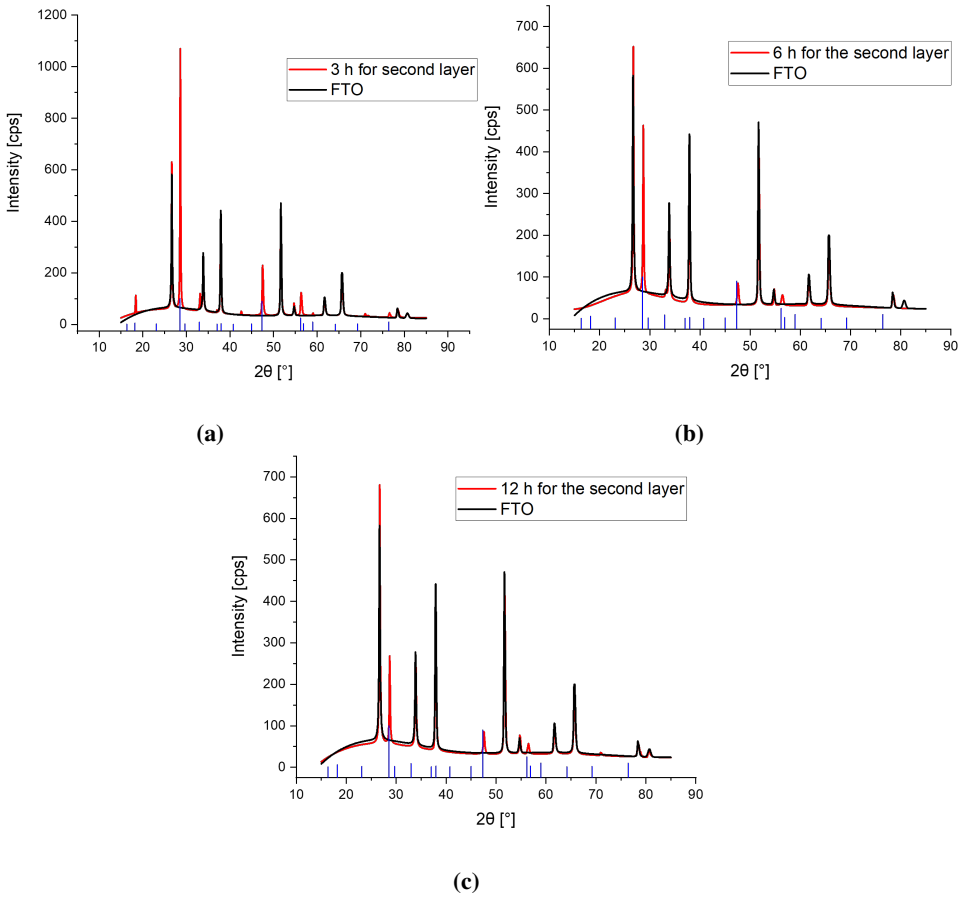

Figure 4.22: X-ray diffractograms for two-layered samples with fixed dip angle and annealed **(a)** 3 h for the second layer, **(b)** 6 h for the second layer and **(c)** 12 h for the second layer. All three diffractograms include a clean FTO measurement and solid blue lines for known XRD peaks of CZTS (PDF card no. 00-026-0575).

The highest intensity for the largest peak in CZTS was seen in fig.4.22a and also shows peaks at 18.2°, 33.0°, 47.5°, 56.3°, 59.0° and 76.6°; which indicated the most prevalence of CZTS in the two-layered sample annealed 3 h for the second layer. Apart from the largest peak at 28.7° in fig.4.22b and fig.4.22c, only peaks at 47.6° and 56.4° were also seen in the diffractograms, with an additional minor peak in the latter diffractogram at 70.9°. The small peak at 70.9° could have belonged to ZnS, Cu_2SnS_3 or CZTS.

UV-VIS spectra for two-layered samples with fixed dip angle and annealing time of 3 h, 6 h and 12 h for the second layer are shown in fig.4.23a, fig.4.23b and fig.4.23c respectively. All three UV-VIS spectra showed absorption in the 600-800 nm range, which

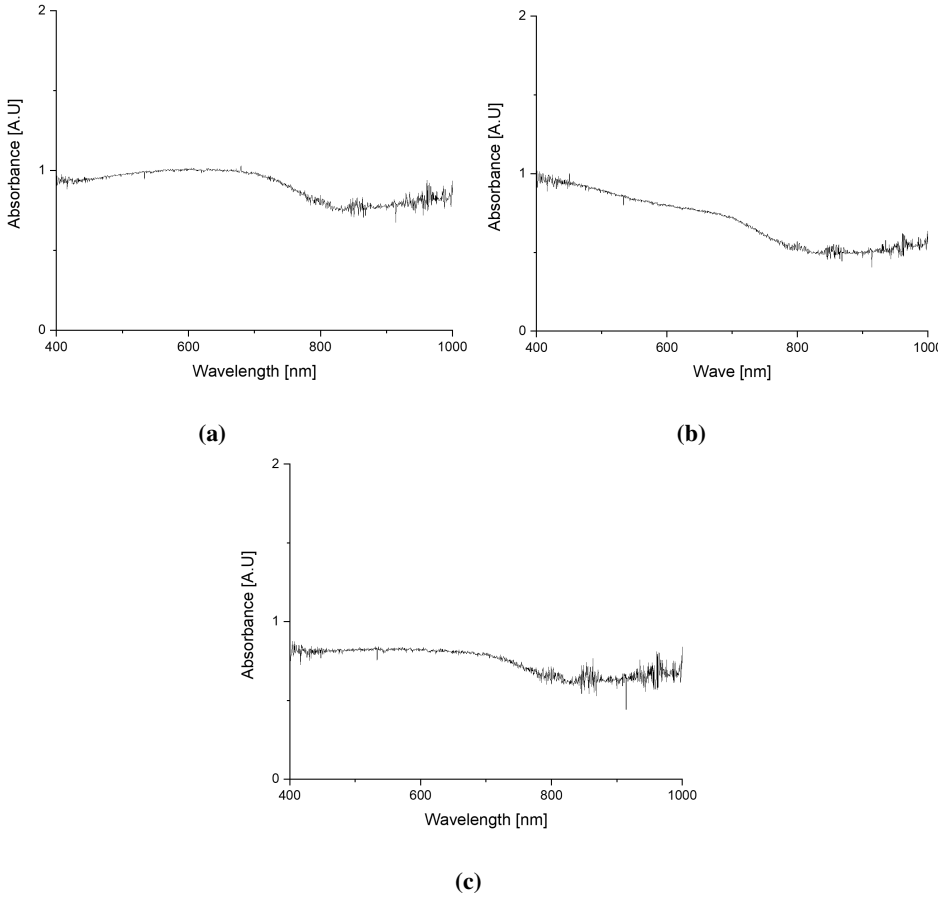

Figure 4.23: UV-VIS spectra for two-layered samples with fixed dip angle and annealed **(a)** 3 h for the second layer, **(b)** 6 h for the second layer and **(c)** 12 h for the second layer.

indicated absorption within the largest section of terrestrial radiance, as seen in fig. 2.2

Surface SEM images in low and high resolution of two-layered samples with fixed dip angle and annealing time of 3 h, 6 h and 12 h for the second layer are shown in figs.4.24a and 4.24b, figs.4.25a and 4.25b, and figs.4.26a and 4.26b respectively.

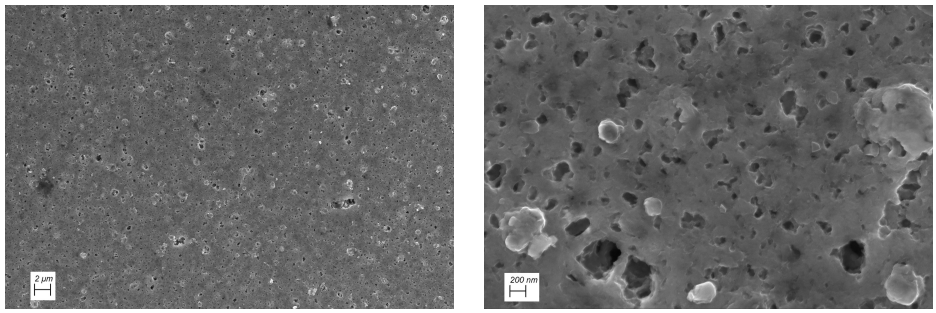

(a) **(b)**

Figure 4.24: Surface SEM images of a two-layered sample with fixed dip angle and annealed 3 h for the second layer at **(a)** low resolution and **(b)** high resolution.

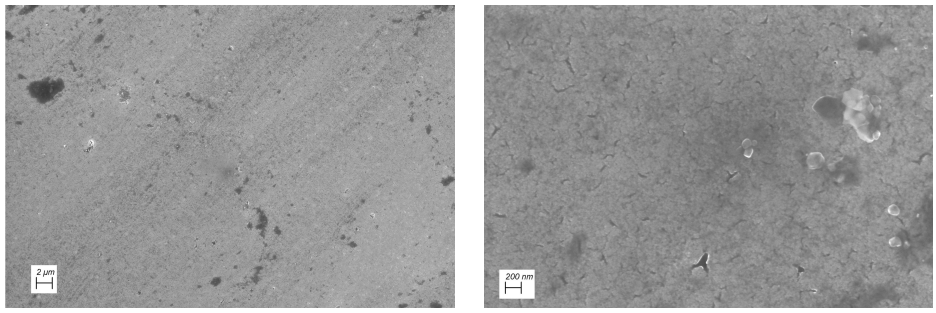

(a) **(b)**

Figure 4.25: Surface SEM images of a two-layered sample with fixed dip angle and annealed 6 h for the second layer at **(a)** low resolution and **(b)** high resolution.

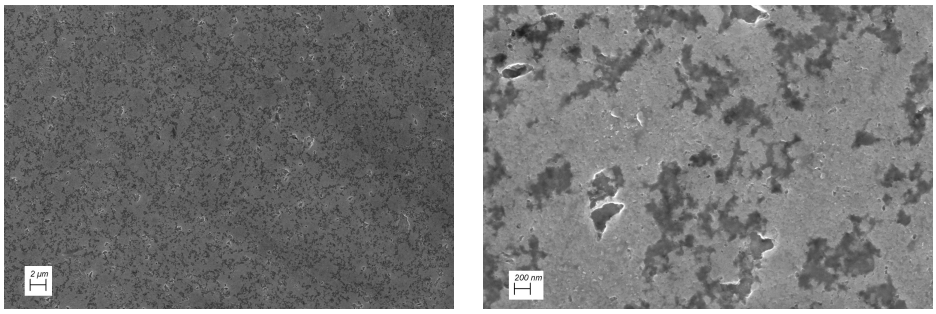

(a) **(b)**

Figure 4.26: Surface SEM images of a two-layered sample with fixed dip angle and annealed 12 h for the second layer at **(a)** low resolution and **(b)** high resolution.

The surface SEM images of two-layered samples with fixed dip angles in fig.4.24a, fig.4.25a and 4.26a showed little no crystallites on the surface. The two-layered sample annealed at 6 h for the second layer displayed the lowest degree of porosity comparing the higher resolutions of all three two-layered samples with fixed dip angles in fig.4.24b, fig.4.25b and fig.4.26b. This could have indicated that a higher rate of grain growth occurred for a two-layered sample annealed 6 h for the second layer, compared to 3 h or 12 h for the second layer. The two-layered sample annealed 3 h for the second layer in fig.4.24b, appeared to have more pinholes in the film than the other three and the highest amount of crystallites on the surface which could have indicated the highest degree of secondary phases or polymorphs of CZTS. The secondary phases could have been responsible for a reduced grain growth and left the bulk as a volatile compound during annealing, thus formed the pinholes in the film.

Cross-sectional SEM image, EDXS line scan and element mapping for the two-layered sample with fixed dip angle and annealed 3 h for the second layer can be seen in fig. 4.27a, fig. 4.27b and fig. 4.27c respectively. The cross-section SEM image in fig. 4.27a showed a measured thickness of around 610 nm, and the EDXS line scan in fig. 4.27b showed a measured thickness of around 810 nm and 880 nm for the intersections of the sulfur signal with the tin and oxygen signal respectively. The EDXS sulfur map

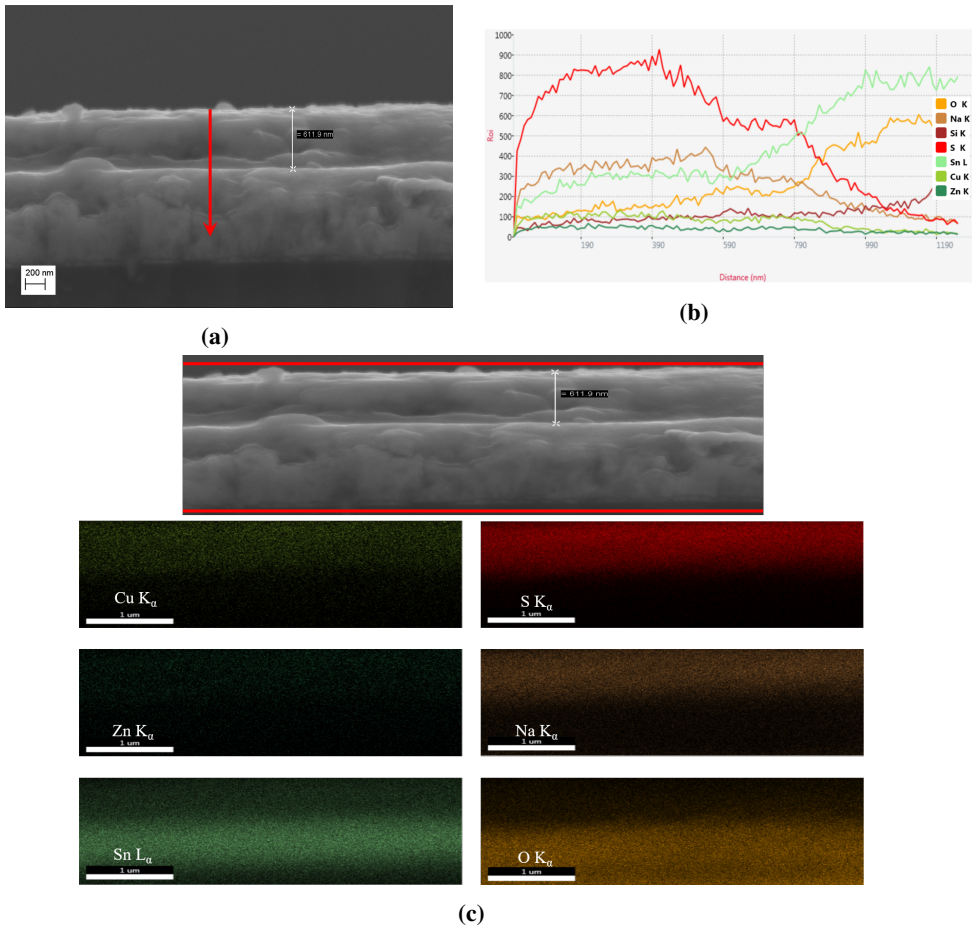

Figure 4.27: **(a)** Cross-section SEM image of a two-layered sample with fixed withdrawal speed and annealed 3 h for the second layer. The red vertical line marks line scan position. **(b)** Cross-section EDXS line scan oriented from surface towards the substrate and **(c)** EDXS element mapping. Red horizontal lines mark the scanning area.

in fig. 4.27c showed a clear separation between the two-layered sample bulk and the substrate, with little to no copper and zinc present in the two-layered sample. Sodium was also present in the two-layered sample which indicated a degree of diffusion from the substrate.
Cross-sectional SEM image, EDXS line scan and element mapping for the two-layered sample with fixed dip angle and annealed 6 h for the second layer can be seen in fig. 4.28a, fig. 4.28b and fig. 4.28c respectively. The cross-section SEM image in fig. 4.28a showed a measured thickness of around 790 nm, and the EDXS line scan in fig. 4.28b showed a measured thickness of around 910 nm and 900 nm for the intersections of the sulfur signal with the tin and oxygen signal respectively. The EDXS sulfur map in fig. 4.28c showed a clear separation between the two-layered sample bulk and the substrate, with little to no copper and zinc present in the two-layered sample. Sodium was only slightly also present in the two-layered sample which indicated a minimal degree of diffusion from the substrate.

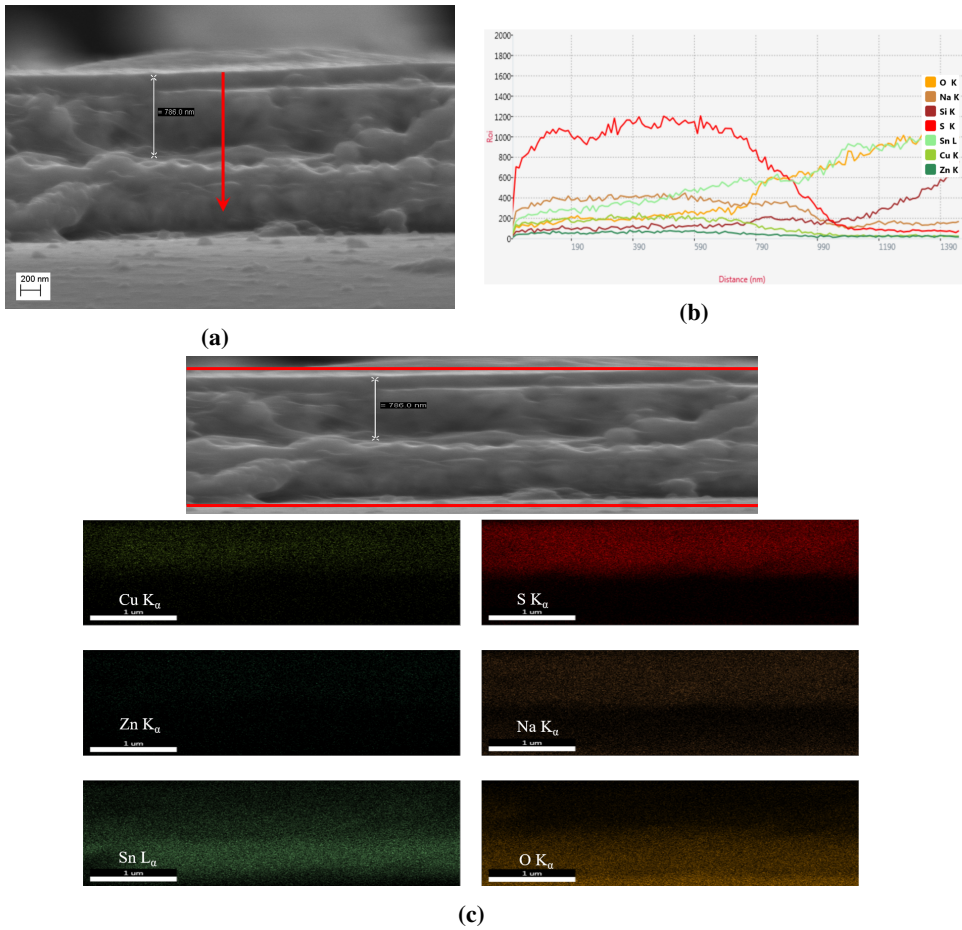

Figure 4.28: **(a)** Cross-section SEM image of a two-layered sample with fixed withdrawal speed and annealed 6 h for the second layer. The red vertical line marks line scan position. **(b)** Cross-section EDXS line scan oriented from surface towards the substrate and **(c)** EDXS element mapping. Red horizontal lines mark the scanning area.

Cross-sectional SEM image, EDXS line scan and element mapping for the two-layered sample with fixed dip angle and annealed 12 h for the second layer can be seen in fig. 4.29a, fig. 4.29b and fig. 4.29c respectively. The cross-section SEM image in fig. 4.29a showed a measured thickness of around 760 nm, and the EDXS line scan in fig. 4.29b showed a measured thickness of around 530 nm and 610 nm for the intersections of the sulfur signal with the tin and oxygen signal respectively. The EDXS sulfur map in fig.

4.29c showed a clear separation between the two-layered sample bulk and the substrate, with clear appearance of copper and some zinc in the two-layered sample. Sodium was also quite present in the two-layered sample which indicated a larger degree of diffusion from the substrate.

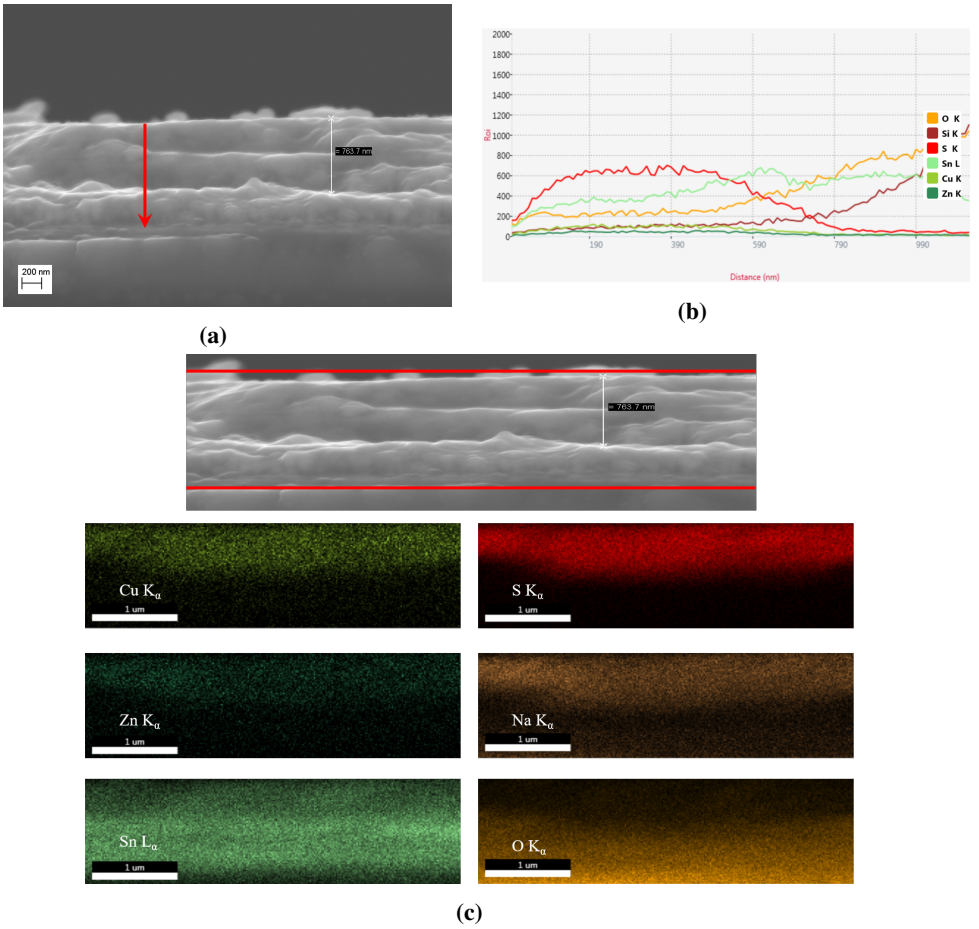

Figure 4.29: **(a)** Cross-section SEM image of a two-layered sample with fixed withdrawal speed and annealed 12 h for the second layer. The red vertical line marks line scan position. **(b)** Cross-section EDXS line scan oriented from surface towards the substrate and **(c)** EDXS element mapping. Red horizontal lines mark the scanning area.

Table 4.5 shows the measured thicknesses of two-layered samples with fixed withdrawal speed, fixed dip angle and an annealing time of 3 h, 6 h, or 12 h for the second layer using different sources to calculate and average thickness value.

Table 4.5: Measured thicknesses for two-layered samples with fixed withdrawal speed and fixed dip angles, and annealing time for the second layer of 3 h, 6 h, or 12 h. The sources of data were cross-sectional SEM images and EDXS line scans, where the latter applied the distance to the intersection between the sulfur signal and the tin or oxygen signal. All measurements and averages are rounded to nearest 10 nm.

	Measured thickness [nm] $\pm$10 nm			
Annealing time for the second layer [h]	Cross-section SEM	Cross-section EDXS line scan using Sn signal	Cross-section EDXS line scan using O signal	Average [nm] $\pm$30 nm
3	610	810	880	770
6	790	910	900	870
12	760	530	610	630

Considering the average thickness values in table 4.5, there was an increased sample thickness from 3 h to 6 h annealing time for the second layer, and then a decreased from 6 h to 12 h for the second layer, which reached an overall minimum among the three two-layered samples.

Tauc plots for two-layered samples with fixed dip angle and annealed 3 h, 6 h or 12 h for the second layer can be seen in fig. 4.30a, fig. 4.30b and fig. 4.30c respectively. The estimated bandgap values for the two-layered samples with fixed dip angle and annealed 3 h, 6 h or 12 h for the second layer were 1.42 eV, 1.52 eV and 1.43 eV respectively. These values were close to the expected bandgap value for CZTS which is around 1.5 eV.

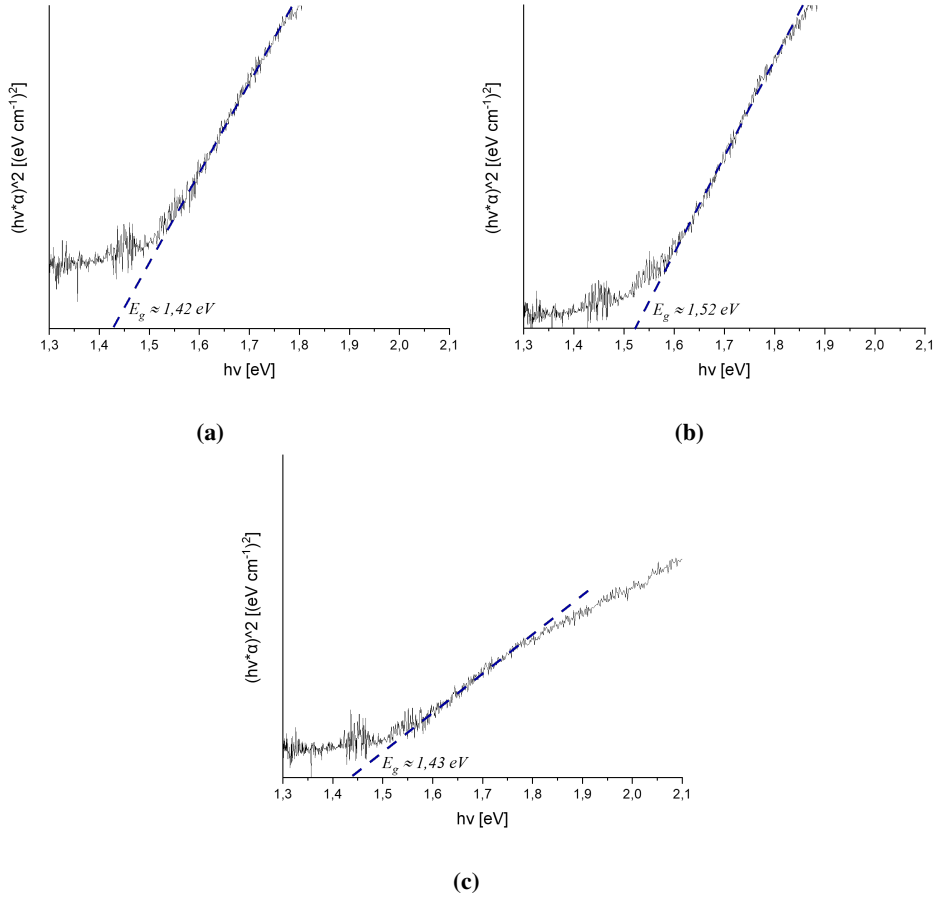

Figure 4.30: Tauc plots for two-layered samples with fixed dip angle and annealed **(a)** 3 h for the second layer, **(b)** 6 h for the second layer and **(c)** 12 h for the second layer. Calculations were done with average thickness values in table 4.5

Chapter 5

Discussion

5.1 Dip-coating

5.1.1 The influence of withdrawal speed

The deposited thickness of the film appears to be dependent on an increase of withdrawal speed. Since the increase in thickness is evident, it is possible that the range of withdrawal speeds is within the Landau-Levich regime. The samples that had different withdrawal speed showed this trend in their Raman spectra (fig. 4.1 and fig. 4.2), in their X-ray diffractograms (fig. 4.3a and fig. 4.3b) and in their UV-VIS spectra (fig. 4.4a and fig. 4.4b). It remains however uncertain exactly where within the Landau-Levich regime the withdrawal speeds operated within. The regime is dependent on the physiochemical properties of the precursor solution and would therefore likely vary from one batch to another, depending on the precision of measurements used. The highest withdrawal speed used was the maximum withdrawal speed that could be used by the in-house built dip-coater. However, considering that the Landau-Levich regime has been considered to be applicable for liquids with low viscosity and withdrawal speeds from around 1 cm min^{-1} to 10 cm min^{-1}[46], it would be reasonable to assume that the upper limit of sample thickness is close when operating at a withdrawal speed of 30 cm min^{-1}. At this limit, the sample thickness stagnates towards a practical maximum value as the capillary forces can no longer compete with the gravitational forces involved.[73]
The surface SEM images for the two highest withdrawal speeds (fig. 4.5b and fig.4.6b) showed an increased amount crystallites on the surface as the withdrawal speed increased. It could be possible that an increased film thickness would enable a higher nucleation rate of secondary phases or polymorphs of CZTS, as the amount of reactants would be proportional with said deposited film thickness.

5.1.2 Coating composition and homogeneity

The use of Kapton to form stencils for the dip-coating deposition improved the film quality drastically, from originally appearing as ring-formed films to forming homogeneous films. The problem is commonplace for experiments involving drying of droplets to form films.[92] The evaporation flux of sessile droplets will be highest at the edges and so capillary action will cause the solution to move out towards the edge, maintaining the contact line.[93] Any solutes will therefore be concentrated towards the edge of the drop, forming a ring-shaped film after complete evaporation. However, the issue could be avoided if the evaporation flux is more uniform across the deposited film. The Kapton could possibly have affected the contact angle at the edges of the deposition, resulting in a more uniform evaporation across the surface of the film. This possibility would imply that capillary action will no longer concentrate solutes towards any direction, resulting in an uniform spreading of solutes.
The surface SEM images of samples annealed 1 h for each layer, both one and two-layered samples, showed the presence of crystallites on the surface, which were not present on the surface of the two-layered sample annealed 12 h for each layer. This might suggest that for a two layered sample, a total annealing time between 2 h and 24 h could result in the loss of said crystallites. The degree of porosity also increased with the annealing time for each layer possibly suggesting an inhibited grain growth during annealing or loss of volatile compounds during annealing forming holes in the film structure. It remained uncertain however if within the aforementioned total annealing time range of 2 h to 24 h that the onset of increased porosity occurs after the loss of crystallites on the surface or during the loss of crystallites no the surface. It is likely that the two mechanisms occur at the same time, as the crystallites could have recrystallized or escaped the bulk structure in gaseous states during the annealing, as previously mentioned. The surface SEM images were also taken with different accelerating voltages but were not specified for each picture, as it would not affect the phases present but vary the grey scale of the image. A surface SEM image of a clean FTO substrate was also used to ensure that the viewed surface was the deposited sample, and not the substrate. The surface SEM image of the clean FTO sample can be seen in the appendix (fig. 7.1).
The surface EDXS element mapping (fig. 4.7) gave no clear indication as to what the crystallites were, but that it likely stood between a ternary phase like Cu_2SnS_3 or possibly a different polymorph of CZTS compared the bulk structure. Based on the results of the Raman spectra, it appeared as if there were secondary phases in the samples, which could be the crystallites seen on the surface or possibly phases inside the bulk structure of the sample. The Raman spectra suggested the presence of CZTS, Cu_2SnS_3 and Sn_2S_3, because $Cu_{2-X}S$ and SnS were less likely considering how only one of their peaks were seen in the spectra. The Raman spectra were simply not clear enough to establish a pres-

ence of possible polymorphs of CZTS or distinguish the peaks of Cu_2SnS_3 and Sn_2S_3 as they could be convoluted by the main peaks of CZTS. The Raman spectra show no signs of ZnS being present but ZnS is however known to have a lower scattering effect at higher excitation wavelengths.[94] The choice of excitation wavelength for Raman analysis reflects that a higher wavelength can penetrate deeper into a sample. Considering the targeted thickness being 1 μm, a high excitation wavelength would be required to be able to analyze the entire sample. The UV-VIS spectra of the two-layered samples with fixed withdrawal speed (fig.4.10) show a different absorption range for the samples annealed at 1 h each layer, and the sample annealed at 12 h each layer. This further indicates that there could be different phases present in the two samples. In the X-ray diffractograms, a shift in the major peak towards a lightly higher angle could be caused by the presence of ZnS[95], but is difficult to determine as the major peaks of ZnS are almost identical to those of CZTS.[90][95][96] The presence of Cu_2SnS_3 in CZTS has been reported to show a shift of major peaks towards lower angles of the major peak.[95], but like ZnS, it is also difficult to distinguish as the major peaks are almost identical to those of CZTS[90][95] The X-ray diffractograms support the presence of Cu_2SnS_3 and ZnS in the sample, as well as ruling out any signs of Sn_2S_3, and so the likely result is that the two-layered sample annealed 1 h for each layer contains a CZTS bulk with possible ZnS phases, and the crystallites on the surface are possibly the ternary phase Cu_2SnS_3. The two-layered sample annealed 12 h for each layer on the other hand contains a CZTS bulk with possible ZnS phases.
When utilizing the cross-section EDXS line scans for thickness measurements, the signal intersections of the most abundant element present in the sample and the substrate would be a reasonable choice. These elements should be sulfur in the sample, while tin and oxygen should be most abundant in the substrate. The cross-section SEM image generally show a completely different thickness value compared to the EDXS line scans. It is however important to consider how the EDXS measures the prevalence of elements in a sample. The penetration volume of the electrons 15 kV is likely to be marginally larger than the resolution used for the line scans which was 10 nm.[97] This could be causing one measurement step in the line scan to have contributions from many neighbouring measurement steps. The result is that a measurement step in the FTO substrate would still detect sulfur if the measurement step is close enough to the boundary between sample and substrate. Also, initial dips in the EDXS line scans could be caused by any crystallites on the surface rich in any element compared to the sample bulk. The tin an oxygen signals could be affected by what appears as empty grooves between the substrate and the two-layered sample, further affecting the validity of the thickness measurements of the cross-section EDXS line scans. The cross-section SEM image for the sample annealed 12 h for each layer shows plane mismatch between the substrate and the two-layered sample, most likely caused by an uneven cut, but questions the validity of the thickness measurements of the cross-section SEM images. The discrepancy between the thickness measurements between cross-section SEM images and EDXS line scans is

however not enough cause to disregard enitrely the use of said methods to measure sample thickness. It could be reasonable to assume that the thickness of two-layered samples annealed 1 h or 12 h for each layer to be within the same approximate thickness, and so an average value could be applied to achieve an unbiased estimation. It is however safe to assume that none of the two-layered samples reached a thickness of at least 1 μm.
The thickness values are necessary for computing the absorption coefficient values in the respective Tauc plots. It is however worth mentioning that even a difference of more than 250 nm resulted in a change of 0.1 eV in the bandgap value for the two-layered sample annealed 12 h for each layer. The difference is therefore minimal and has little effect on the final bandgap estimation for the sample.
The cross-section EDXS element mapping shows the top layer being rich in sulfur, and including copper, tin and zinc, indicating the presence of CZTS. The element mapping does not show any clear secondary phases in the two-layered sample bulk that are rich in any particular element, as every element in the two-layered samples appeared to be evenly spread. The underlying layer has a much higher tin and oxygen prevalence, indicating the presence of FTO. The sulfur map being most intense in the top layer, shows possible diffusion of sulfur across the boundary and into the substrate. The oxygen map does likewise from the bottom layer into the top layer. The cause of both could be diffusion from each their respective layer, but the oxygen signal could be atoms adhered to the sample as it has been in contact with air. This effect could possibly also be responsible for the oxygen intensity being higher than the copper and zinc intensities in the cross-section EDXS line scans of the two-layered samples annealed 1 h or 12 h each layer. The spreading of elements across the boundary is more pronounced in the latter where sodium is quite prevalent in the top layer, and oxygen still is somewhat prevalent in the top layer. The sodium prevalence can not be explained by adhesion of atmospheric gases on the sample, but rather from the SLG layer on which the FTO lays on. Sodium has however been reported to increase grain growth.[59] It is possible that the effect occurs in the two-layered sample annealed 1 h each layer, but the degree of sodium inclusion could be too low for the cross-section EDXS line scan to include it. If the sodium prevalence increases further to the degree found in the two-layered sample annealed 12 h for each layer, the sodium could possibly be responsible for inhibiting CZTS grain growth. It is also possible that the prolonged annealing time could result in diffusion of other elements from the SLG layer into the top layer, but are still in such low concentrations that the EDXS would not include it.
The Tauc plots for the two-layered samples with fixed withdrawal speed and annealed 1 h or 12 h, estimate bandgap values smaller than what is expected for CZTS; which is around 1.5 eV. The values suggest that the two-layered samples include secondary phases that are responsible for lowering the estimated bandgap value of the two-layered samples. Among the possible secondary phases associated with CZTS synthesis, Cu_2SnS_3[98], Cu_2S[99] and SnS[100] all have bandgap values lower than 1.5 eV, which possibly indicates their presence in the two-layered samples.

5.2 Angle dependent dip-coating

5.2.1 The effect of dip angle

The average thickness values for the samples with fixed withdrawal speed and dip angles of 60 °, 45°, 30°, 20° or 10° appeared to decrease reaching a possible minimum at 30° where the sample might have bee too thin to measure, and then increasing again by further decreasing the dip angle. The trend follows the theory in equation 2.10 except that the thickness was expected to be larger at a dip angle of 10 ° than at a dip angle of 60 ° compared to other literature[77][78]. The two-layered samples with fixed withdrawal speed and fixed dip angle did however produce the thicker samples, measured on average, compared to the two-layered samples with fixed withdrawal speed and no altered dip angle. As previously mentioned, there is a large discrepancy between the values measured by the cross-section SEM image and the cross-section EDXS line scans, and so determining the optimal dip angle from the data in the two mentioned methods becomes difficult. The fact remains however that with the in-house built set piece permitting angle dependent dip-coating, any lower dip-angles would cause the entire substrate to submerge as the immersion speed and withdrawal had to be kept the same. The immersion and withdrawal speeds had to be kept the same due to the manual setting of speeds on the in-house built dip-coater. In addition, the use of double-sided tape to attach the substrates to the set piece permitting angle dependent dip-coating resulted in an involuntary, quick removal of the substrate from the tape. This quick removal may have affected the distribution of precursor solution on the substrate, thus changing the overall thickness of the film.

5.2.2 Coating composition and homogeneity

The Raman spectra of the two-layered samples with fixed withdrawal speed and fixed dip angle only indicated the presence of CZTS and $Cu_{2-X}S$, but the presence did diminish by increasing annealing time for the second layer. X-ray diffractograms showed that the lowest annealing time for the second layer, being 3 h, had the most intense peaks indicating the highest prevalence of CZTS among the two-layered samples. However the same diffractogram exhibits minor peaks at angles that do not correspond to the known CZTS peaks, further indicating the presence of secondary phases. As was the case with the two-layered samples annealed for 1 h or 12 h for each layer, neither the Raman spectra nor the X-ray diffractograms could rule out the possibility of having ZnS or Cu_2SnS_3 in the two-layered samples annealed 3 h, 6 h or 12 h for the second layer. The surface SEM image of the same sample supported this possibility as there appeared to be some crystallites on the surface. The surface SEM images of the two-layered samples show an optimal total annealing time of 6.5 h for a two-layered. This does confirm the suspicion mentioned earlier regarding a possible optimal annealing time window where the grain growth is maximized to reach a compact surface with a minimum the amount of

secondary phases present on the surface.
The cross-section EDXS element maps showed a clear presence of sulfur, but a lacking prevalence of zinc and some copper. The EDXS line scans do however show that zinc and copper are present in the two-layered samples, and so the lack of prevalence in the EDXS element mapping could be a result of a poor contrast. Similar to the two-layered samples annealed 1 h or 12 h each layer, the element mapping also confirms that there appears to be no large grains of secondary phases in the bulk of the sample, as every element in the two-layered samples annealed 3 h, 6 h or 12 h for the second layer are evenly spread. Due to the poor contrast, it is difficult to say if the sodium prevalence increases with annealing time thus affecting grain growth, but the fact remains a possibility as the surface SEM image for the two-layered sample annealed 12 h for the second layer exhibits a certain degree of porosity.
The average thickness values for the two-layered sample annealed for 3 h, 6 h or 12 h, appears to increase with the total annealing time, reaching a maximum for a total annealing time of 6.5 h and then decreasing again to reach an overall minimum after a total annealing time of 12.5 h. The same trend is also the case for the two-layered samples annealed 1 h or 12 h for each layer, where the film thickness increases from a total annealing time of 2 h to 24 h. It does not seem likely that the CZTS bulk would undergo a phase transformation at 500 °C as it has been reported to undergo transition at around 300 °C [101][102] and another phase transition at around 850 °C.[103] The trend could simply be affected by the large discrepancy of the different thickness measurements and further affecting the degree of uncertainty for the average values. It is however safe to assume that none of the two-layered samples reached a thickness of at least 1 μm.
The Tauc plots for the two-layered samples with fixed withdrawal speed and fixed dip-angle with an annealing time of 3 h, 6 h or 12 h for the second layer, had estimated bandgap values quite close to what is expected for CZTS; which is around 1.5 eV. The values suggested that the two-layered samples annealed at 3 h and 12 h for the second layer include secondary phases that are responsible for lowering the estimated bandgap value, as these two-layered samples had estimated bandgap values of 1.42 eV and 1.43 eV respectively. Among the possible secondary phases associated with CZTS synthesis, Cu_2SnS_3[98], chCu2S[99] and SnS[100] have bandgap values lower than 1.5 eV, which possibly indicates their presence in the two-layered samples. The two-layered sample annealed 6 h for the second layer displayed an estimated bandgap of 1.52 eV which can be considered within an acceptable range of the expected bandgap value.

Chapter 6

Conclusion

The aim of this work was to investigate the optimal parameters for synthesis of thin film kesterites by dip-coating for photovoltaic applications. The parameters that were to be investigated included withdrawal speed, annealing time and dip angle of substrate. By means of post-synthesis analysis, properties that were to be investigated included surface morphology, thin film thickness, phase purity, element distribution, as well as bandgap energy estimations. The methods of analysis included Raman spectroscopy, X-ray diffraction, UV-VIS absorption, surface and cross-section SEM imaging, as well as surface EDXS element mapping and cross-section EDXS line scans and element mapping.

Samples were produced my means of dip-coating at different withdrawal speed and displayed a CZTS thin film with possible ZnS phases in the bulk and crystallites on the surface believed to be Cu_2SnS_3. The films increased in thickness by increasing withdrawal speed, and average thickness values of around 720 nm and 790 nm were calculated for two-layered samples that were produced with fixed withdrawal speeds of 30 cm min^{-1} and annealed 1 h or 12 h for each layer respectively. The same two-layered samples had estimated bandgap values of 1.30 eV and 1.32 eV respectively, and showed an even distribution of elements with a higher porosity for the latter.

Samples were also produced by means of angle dependent dip-coating with different dip angles and showed a decrease in thickness by decreasing the dip angle, until reaching a minimum where the sample thickness increased again as the dip angle was decreased further. Average thickness values of around 880 nm, 900 nm and 610 nm were calculated for two-layered samples with fixed withdrawal speed, fixed dip angle and a fixed annealing time of 0.5 h for the first layer, but 3 h, 6 h or 12 h for the second layer respectively. The same two-layered samples had estimated bandgap values of 1.42 eV, 1.52 eV and 1.43 eV respectively, and showed an even distribution of elements. The two-layered

sample with a total annealing time of 6.5 h displayed the smallest degree of porosity and minimal amount of crystallites on the surface which were also believed to be Cu_2SnS_3, with a possibility of ZnS phases in the bulk.
The experimental procedure involving the use angle dependent dip-coating has been deemed a more fitting method of producing CZTS compact films with most acceptable bandgap values, thickest samples and a lower porosity compared to the experimental procedure involving the use of conventional dip-coating. After two depositions, none of the films were not deemed to reach a thickness of at least 1μm and were not, with certainty, entirely phase pure, however these issues do not seem detrimental to the fact that CZTS thin films were successfully synthesized by means of dip-coating and angle dependent dip-coating.

Chapter 7

Further work

Establishing the optimal annealing time while employing the same experimental procedure could ensure a compact film with little to no secondary phases in the sample. This could be done by producing samples with the same experimental procedure and investigating annealing times between 4 h and 10 h. When an optimal annealing time has been established, the temperature used could also be a new parameter to optimize, using the same approach as mentioned, and investigating annealing temperatures between 450 °C and 550 °C. Also using Raman spectrometers with lower excitation wavelengths could help decide whether ZnS is present or not.

Regarding the use of angle dependent dip-coating, an alternative attachment mechanism would be beneficial for the reproducibility of the procedure and make it clearer to establish whether angle-dependent dip-coating could be employed for an up-scaled production and synthesis of CZTS thin films.

Another possible solution-based sulfur source that has been investigated is similar to thiourea, namely thioacetamide. Thioacetamide is structurally similar to thiourea, with exception of one methyl group being substituted by an amine group. Investigating the use of this compound as a solution-based sulfur source could prove beneficial to the experimental procedure.

Bibliography

(1) OECD/IEA *International Energy Agency. Global Energy & CO2 Status Report 2017*; tech. rep. March; 2018, pp 1–14.

(2) Green, M. A., *Solar cells: operating principles, technology, and system applications*; Prentice-Hall series in solid state physical electronics; Prentice-Hall: 1982.

(3) Philipps, S. *Photovoltaics Report, updated: 27 August 2018*; tech. rep. August; Freiburg: Fraunhofer Institute for Solar Energy Systems, ISE, 2018.

(4) Benick, J.; Richter, A.; Müller, R.; Hauser, H.; Feldmann, F.; Krenckel, P.; Riepe, S.; Schindler, F.; Schubert, M. C.; Hermle, M.; Bett, A. W.; Glunz, S. W. *IEEE Journal of Photovoltaics* **2017**, *7*, 1171–1175.

(5) Liu, F.; Yan, C.; Huang, J.; Sun, K.; Zhou, F.; Stride, J. A.; Green, M. A.; Hao, X. *Advanced Energy Materials* **2016**, *6*, 1600706.

(6) Tajima, S.; Itoh, T.; Hazama, H.; Ohishi, K.; Asahi, R. *Applied Physics Express* **2015**, *8*, 082302.

(7) Jin, X.; Yuan, C.; Jiang, G.; Liu, W.; Zhu, C. *Materials Letters* **2016**, *175*, 180–183.

(8) Sánchez, T. G.; Mathew, X.; Mathews, N. R. *Journal of Crystal Growth* **2016**, *445*, 15–23.

(9) Ananthoju, B.; Mohapatra, J.; Jangid, M. K.; Bahadur, D.; Medhekar, N. V.; Aslam, M. *Scientific Reports* **2016**, *6*, 35369.

(10) Todorov, T. K.; Reuter, K. B.; Mitzi, D. B. *Advanced Materials* **2010**, *22*, E156–E159.

(11) Tao, J.; Chen, L.; Cao, H.; Zhang, C.; Liu, J.; Zhang, Y.; Huang, L.; Jiang, J.; Yang, P.; Chu, J. *Journal of Materials Chemistry A* **2016**, *4*, 3798–3805.

(12) Kermadi, S.; Sali, S.; Ait Ameur, F.; Zougar, L.; Boumaour, M.; Toumiat, A.; Melnik, N. N.; Hewak, D. W.; Duta, A. *Materials Chemistry and Physics* **2016**, *169*, 96–104.

(13) Shinde, N. M.; Lokhande, C. D.; Kim, J. H.; Moon, J. H. *Journal of Photochemistry and Photobiology A: Chemistry* **2012**, *235*, 14–20.

(14) Phan Thi, K. L.; Anh Tuan, D.; Huu Ke, N.; Anh Le, T. Q.; Hung, L. V. T. *Journal of Sol-Gel Science and Technology* **2017**, *83*, 324–331.

(15) Aslan, F.; Tumbul, A. *Journal of Alloys and Compounds* **2014**, *612*, 1–4.

(16) Tumbul, A.; Göktaş, A.; Zarbali, M. Z.; Aslan, F. *Materials Research Express* **2018**, *5*, 066408.

(17) Sun, Y.; Zhang, Y.; Wang, H.; Xie, M.; Zong, K.; Zheng, H.; Shu, Y.; Liu, J.; Yan, H.; Zhu, M.; Lau, W. *Journal of Materials Chemistry A* **2013**, *1*, 6880–6887.

(18) Patel, K.; Kheraj, V.; Shah, D. V.; Panchal, C. J.; Dhere, N. G. *Journal of Alloys and Compounds* **2016**, *663*, 842–847.

(19) Chaudhuri, T. K.; Tiwari, D. *Solar Energy Materials and Solar Cells* **2012**, *101*, 46–50.

(20) Nelson, J., *The Physics of Solar Cells*; Imperial College Press: London, 2003, p 363.

(21) Coddington, O.; Lean, J. L.; Pilewskie, P.; Snow, M.; Lindholm, D. *Bulletin of the American Meteorological Society* **2016**, *97*, 1265–1282.

(22) Kopp, G.; Lean, J. L. *Geophysical Research Letters* **2011**, *38*, n/a–n/a.

(23) Gueymard, C. A.; Myers, D.; Emery, K. *Solar Energy* **2002**, *73*, 443–467.

(24) National Renewable Energy Laboratory Solar Spectra — Grid Modernization — NREL.

(25) West, A. R., *Solid State Chemistry*, 2nd; John Wiley & Sons, Ltd: 2014, p 556.

(26) Kittel, C., *Introduction to Solid State Physics*, 8th ed.; Wiley: 2004, p 704.

(27) Subba Ramaiah Kodigala, *Thin Film Solar Cells from Earth Abundant Materials Growth and Characterization of*; Elsevier: 2014, p 187.

(28) El Chaar, L.; Lamont, L. A.; El Zein, N. Review of photovoltaic technologies., 2011.

(29) Bae, S. H.; Zhao, H.; Hsieh, Y. T.; Zuo, L.; De Marco, N.; Rim, Y. S.; Li, G.; Yang, Y. Printable Solar Cells from Advanced Solution-Processible Materials., 2016.

(30) Jones, R. K.; Ermer, J. H.; Fetzer, C. M.; King, R. R. *Japanese Journal of Applied Physics* **2012**, *51*, 10–11.

(31) Shockley, W.; Queisser, H. J.; Ell, R. *Citation: J. Appl. Phys* **1961**, *32*, 510.

(32) Chiu, P. T.; Law, D. C.; Woo, R. L.; Singer, S. B.; Bhusari, D.; Hong, W. D.; Zakaria, A.; Boisvert, J.; Mesropian, S.; King, R. R.; Karam, N. H. In *2014 IEEE 40th Photovoltaic Specialist Conference, PVSC 2014*, IEEE: 2014, pp 11–13.

(33) Rühle, S. *Solar Energy* **2016**, *130*, 139–147.

(34) Sun, K.; Yan, C.; Liu, F.; Huang, J.; Zhou, F.; Stride, J. A.; Green, M.; Hao, X. *Advanced Energy Materials* **2016**, *6*, 1600046.

(35) Mineralogical Association of Canada., Y.; Koto, K.; Morimoto, N., *The Canadian mineralogist.* 3; Mineralogical Association of Canada: 1978; Vol. 16, pp 397–404.

(36) Ito, K.; Nakazawa, T. *Japanese Journal of Applied Physics* **1988**, *27*, 2094–2097.

(37) Wang, D.; Zhao, W.; Zhang, Y.; Liu, S. (Path towards high-efficient kesterite solar cells., 2018.

(38) Yaroshevsky, A. A. *Geochemistry International* **2006**, *44*, 48–55.

(39) Dimitrievska, M.; Boero, F.; Litvinchuk, A. P.; Delsante, S.; Borzone, G.; Perez-Rodriguez, A.; Izquierdo-Roca, V. *Inorganic Chemistry* **2017**, *56*, 3467–3474.

(40) Chen, S.; Gong, X. G.; Walsh, A.; Wei, S. H. *Applied Physics Letters* **2010**, *96*, 021902.

(41) Scragg, J. J.; Kubart, T.; Wätjen, J. T.; Ericson, T.; Linnarsson, M. K.; Platzer-Björkman, C. *Chemistry of Materials* **2013**, *25*, 3162–3171.

(42) Downs, R.; Hall-Wallace, M. The American Mineralogist Crystal Structure Database., 2003.

(43) Wang, W.; Winkler, M. T.; Gunawan, O.; Gokmen, T.; Todorov, T. K.; Zhu, Y.; Mitzi, D. B. *Advanced Energy Materials* **2014**, *4*, 1301465.

(44) European Chemicals Agency Substance information - Hydrazine., 2019.

(45) Sun, K.; Yan, C.; Huang, J.; Sun, K.; Sun, H.; Jiang, L.; Deng, X.; Stride, J.; Hao, X.; Liu, F. *Journal of Alloys and Compounds* **2018**, *750*, 328–332.

(46) Brinker, C. J. In *Chemical Solution Deposition of Functional Oxide Thin Films*; Springer Vienna: Vienna, 2013; Vol. 9783211993; Chapter 10, pp 233–261.

(47) Nagoya, A.; Asahi, R.; Wahl, R.; Kresse, G. *Physical Review B - Condensed Matter and Materials Physics* **2010**, *81*, DOI: 10.1103/PhysRevB.81.113202.

(48) Olekseyuk, I. D.; Dudchak, I. V.; Piskach, L. V. *Journal of Alloys and Compounds* **2004**, *368*, 135–143.

(49) Prabeesh, P.; Vysakh, K. V.; Selvam, I. P.; Potty, S. N. *Journal of Electronic Materials* **2018**, *47*, 5396–5402.

(50) Wangperawong, A.; King, J. S.; Herron, S. M.; Tran, B. P.; Pangan-Okimoto, K.; Bent, S. F. *Thin Solid Films* **2011**, *519*, 2488–2492.

(51) Madarász, J.; Bombicz, P.; Okuya, M.; Kaneko, S. In *Solid State Ionics*, Elsevier: 2001; Vol. 141-142, pp 439–446.

(52) Kamoun, N.; Bouzouita, H.; Rezig, B. *Thin Solid Films* **2007**, *515*, 5949–5952.

(53) Ki, W.; Hillhouse, H. W. *Advanced Energy Materials* **2011**, *1*, 732–735.

(54) Xin, H.; Katahara, J. K.; Braly, I. L.; Hillhouse, H. W. *Advanced Energy Materials* **2014**, *4*, 1301823.

(55) Su, Z.; Sun, K.; Han, Z.; Cui, H.; Liu, F.; Lai, Y.; Li, J.; Hao, X.; Liu, Y.; Green, M. A. *Journal of Materials Chemistry A* **2014**, *2*, 500–509.

(56) Yu, R. S.; Hung, T. C. *Applied Surface Science* **2016**, *364*, 909–916.

(57) Rakhshani, A. E. *Journal of Alloys and Compounds* **2016**, *675*, 387–392.

(58) Chaudhari, S.; Kannan, P. K.; Dey, S. R. *Thin Solid Films* **2017**, *636*, 144–149.

(59) Prabhakar, T.; Jampana, N. *Solar Energy Materials and Solar Cells* **2011**, *95*, 1001–1004.

(60) Zhuang, X.; Zhang, Y.; Zhang, J.; Chen, Y.; Zhu, Y. *Materials Research Express* **2018**, *6*, DOI: 10.1088/2053-1591/aaeeb2.

(61) Parish, E. J.; Li, S. In *Encyclopedia of Reagents for Organic Synthesis*; John Wiley & Sons, Ltd: Chichester, UK, 2001.

(62) Barta, N. S.; Stille, J. R. In *Encyclopedia of Reagents for Organic Synthesis*; John Wiley & Sons, Ltd: Chichester, UK, 2005.

(63) Trifiletti, V.; Mostoni, S.; Butrichi, F.; Acciarri, M.; Binetti, S.; Scotti., R. *ChemistrySelect* **2019**, *4*, 4905–4912.

(64) Bhosale, S. M.; Suryawanshi, M. P.; Kim, J. H.; Moholkar, A. V. *Ceramics International* **2015**, *41*, 8299–8304.

(65) Ramanujam, J.; Singh, U. P. Copper indium gallium selenide based solar cells - A review., 2017.

(66) Lemire, H. M.; Peterson, K. A.; Sprawls, S.; Singer, K.; Martin, I. T.; French, R. H. In *Reliability of Photovoltaic Cells, Modules, Components, and Systems VI*, ed. by Dhere, N. G.; Wohlgemuth, J. H.; Lynn, K. W., International Society for Optics and Photonics: 2013; Vol. 8825, p 882502.

(67) Yan, Y.; Li, X.; Dhere, R.; Al-Jassim, M.; Jones, K.; Young, M.; Scott, M. In *Conference Record of the IEEE Photovoltaic Specialists Conference*, IEEE: 2010, pp 2519–2521.

(68) Brinker, C. J.; Frye, G. C.; Hurd, A. J.; Ashley, C. S. *Thin Solid Films* **1991**, *201*, 97–108.

(69) Puetz, J.; Aegerter, M. A. In *Sol-Gel Technologies for Glass Producers and Users*; Springer US: Boston, MA, 2004, pp 37–48.

(70) Landau, L.; Levich, V. *Acta Physiochimica* **1942**, *17*, 141–153.

(71) Scriven, L. E. *MRS Proceedings* **1988**, *121*, 717.

(72) Grosso, D. *Journal of Materials Chemistry* **2011**, *21*, 17033–17038.

(73) Faustini, M.; Louis, B.; Albouy, P. A.; Kuemmel, M.; Grosso, D. *Journal of Physical Chemistry C* **2010**, *114*, 7637–7645.

(74) Spiers, R. P.; Subbaraman, C. V.; Wilkinson, W. L. *Chemical Engineering Science* **1975**, *30*, 379–395.

(75) Deryagin, B. M.; Levi, S. M., *Film Coating Theory: The Physical Chemistry of Coating Thin Layers on a Moving Support*; Focal Press: London, 1964, p 190.

(76) Tallmadge, J. A. A theory of entrainment for angular withdrawal of flat supports., 1971.

(77) Bottein, T.; Loizillon, J.; Grosso, D. *Journal of Physical Chemistry B* **2017**, *121*, 6220–6225.

(78) Arfsten, N. J.; Eberle, A.; Otto, J.; Reich, A. *Journal of Sol-Gel Science and Technology* **1997**, *8*, 1099–1104.

(79) Tauc, J.; Grigorovici, R.; Vancu, A. *physica status solidi (b)* **1966**, *15*, 627–637.

(80) Davis, E. A.; Mott, N. F. *Philosophical Magazine* **1970**, *22*, 903–922.

(81) Tauc, J. *Materials Research Bulletin* **1968**, *3*, 37–46.

(82) Viezbicke, B. D.; Patel, S.; Davis, B. E.; Birnie, D. P. *Physica Status Solidi (B) Basic Research* **2015**, *252*, 1700–1710.

(83) Zhou, W.; Apkarian, R.; Wang, Z. L.; Joy, D. In *Scanning Microscopy for Nanotechnology*; Springer New York: New York, NY, 2006, pp 1–40.

(84) Nitsche, R.; Sargent, D. F.; Wild, P. Crystal growth of quaternary 122464chalcogenides by iodine vapor transport., 1967.

(85) ICCD The International Centre for Diffraction Data, www.icdd.com., 2012.

(86) Dimitrievska, M.; Fairbrother, A.; Fontané, X.; Jawhari, T.; Izquierdo-Roca, V.; Saucedo, E.; Pérez-Rodríguez, A. *Applied Physics Letters* **2014**, *104*, 021901.

(87) Liu, T.; Kong, W. J.; Qiao, M.; Cheng, Y. *Results in Physics* **2018**, *11*, 822–825.

(88) Price, L. S.; Parkin, I. P.; Hardy, A. M. E.; Clark, R. J. H.; Hibbert, T. G.; Molloy, K. C. *Chemistry of Materials* **1999**, *11*, 1792–1799.

(89) Munce, C. G.; Parker, G. K.; Holt, S. A.; Hope, G. A. *Colloids and Surfaces A: Physicochemical and Engineering Aspects* **2007**, *295*, 152–158.

(90) Fernandes, P. A.; Salomé, P. M. P.; Cunha, A. F. d. *Journal of Physics D: Applied Physics* **2010**, *43*, 215403.

(91) Zhang, S. Study of fluorine-doped tin oxide (FTO) thin films for photovoltaics applications., Ph.D. Thesis, Université Grenoble Alpes; Technische Universität (Darmtstadt, Germany), 2017.

(92) Routh, A. F. *Reports on Progress in Physics* **2013**, *76*, 046603.

(93) Deegan, R. D.; Bakajin, O.; Dupont, T. F.; Huber, G.; Nagel, S. R.; Witten, T. A. *Nature* **1997**, *389*, 827–829.

(94) Fairbrother, A.; Izquierdo-Roca, V.; Fontané, X.; Ibáñez, M.; Cabot, A.; Saucedo, E.; Pérez-Rodríguez, A. *CrystEngComm* **2014**, *16*, 4120–4125.

(95) Berg, D. M.; Arasimowicz, M.; Djemour, R.; Gütay, L.; Siebentritt, S.; Schorr, S.; Fontané, X.; Izquierdo-Roca, V.; Pérez-Rodriguez, A.; Dale, P. J. *Thin Solid Films* **2014**, *569*, 113–123.

(96) Soltani, N.; Saion, E.; Hussein, M. Z.; Erfani, M.; Abedini, A.; Bahmanrokh, G.; Navasery, M.; Vaziri, P. *International Journal of Molecular Sciences* **2012**, *13*, 12242–12258.

(97) Mendis, B. G. In *Electron Beam-Specimen Interactions and Simulation Methods in Microscopy*; Wiley: Hoboken, New Jersey, 2018; Chapter 2.2, p 296.

(98) Berg, D. M.; Djemour, R.; Gütay, L.; Zoppi, G.; Siebentritt, S.; Dale, P. J. *Thin Solid Films* **2012**, *520*, 6291–6294.

(99) Liu, G.; Schulmeyer, T.; Brötz, J.; Klein, A.; Jaegermann, W. In *Thin Solid Films*, Elsevier: 2003; Vol. 431-432, pp 477–482.

(100) Vidal, J.; Lany, S.; D Avezac, M.; Zunger, A.; Zakutayev, A.; Francis, J.; Tate, J. *Applied Physics Letters* **2012**, *100*, 032104.

(101) Maheshwari, B. U.; Kumar, V. S. *International Journal of Energy Research* **2015**, *39*, 771–777.

(102) Scragg, J. J.; Choubrac, L.; Lafond, A.; Ericson, T.; Platzer-Björkman, C. *Applied Physics Letters* **2014**, *104*, 041911.

(103) Schorr, S.; Gonzalez-Aviles, G. *physica status solidi (a)* **2009**, *206*, 1054–1058.

Appendix

Surface SEM image of a clean FTO substrate is shown in fig.7.1

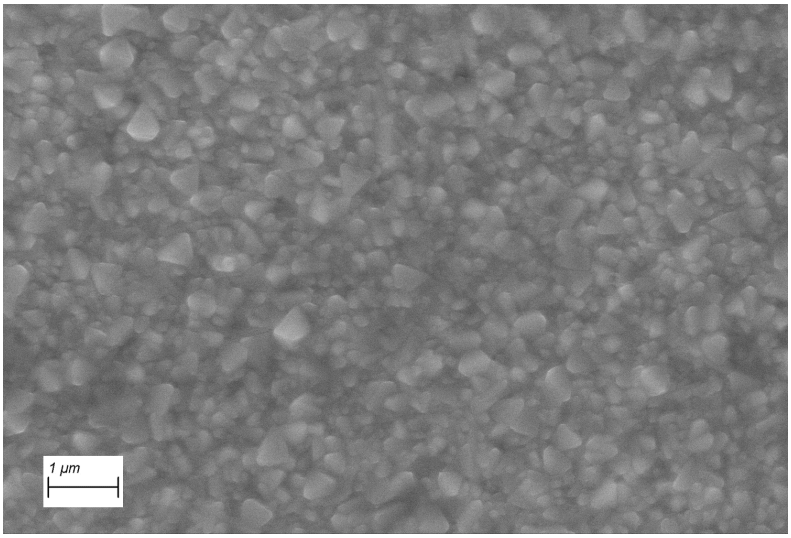

Figure 7.1: Surface SEM image of a clean FTO substrate

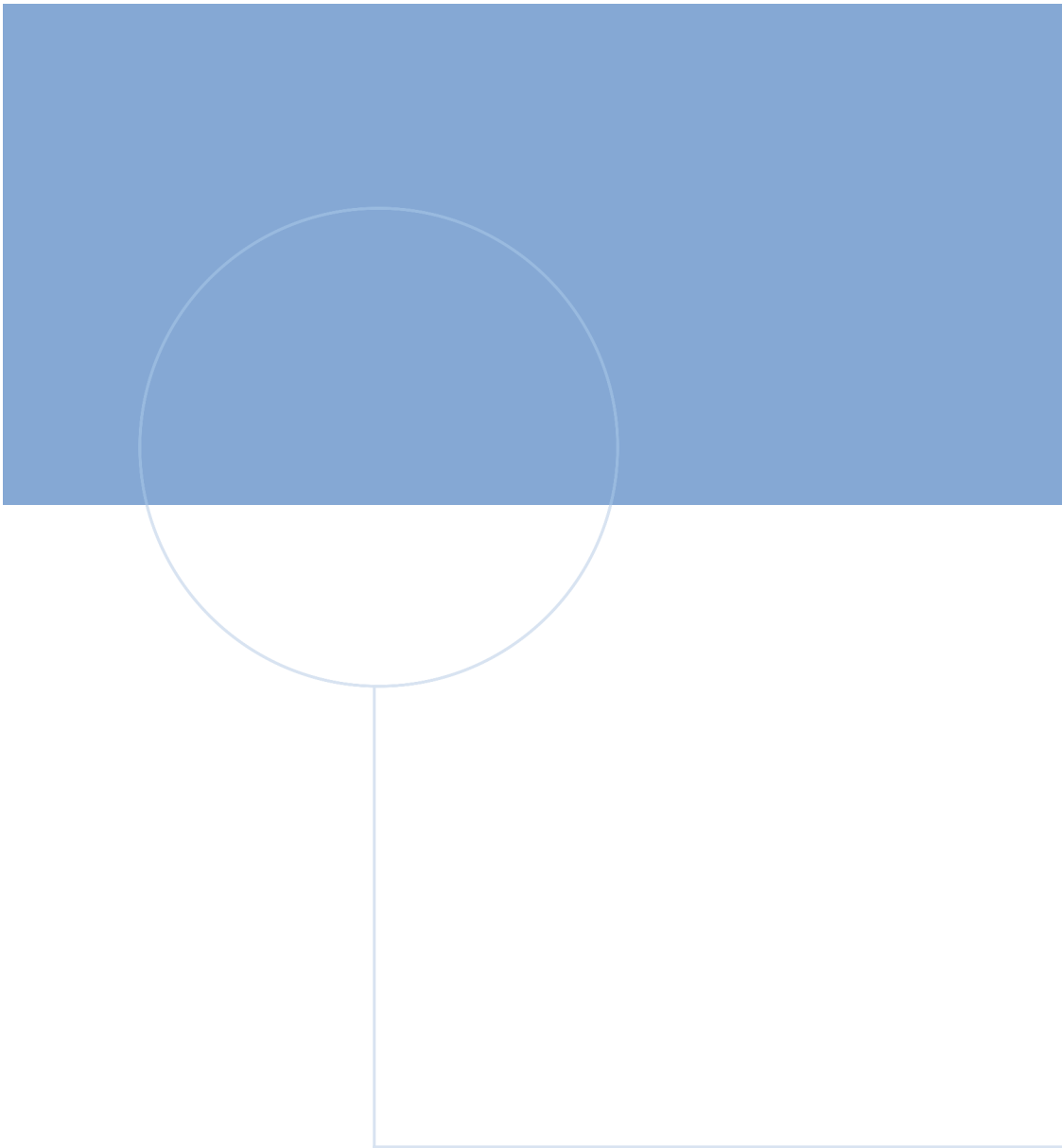

NTNU

Kunnskap for en bedre verden